A global–local approach to predict the fretting-fatigue failure of clamped aluminum powerline conductors: From mono-contact crossed wires to full conductor vibrational tests

Julien Said, Siegfried Fouvry, Georges Cailletaud, Stéphanie Basseville, Marc Coulangeon, Jérôme Brocard, Christine Yang, Fikri Hafid

J. Said, S.Fouvry, G. Cailletaud, S. Basseville, M. Coulangeon, J. Brocard, C. Yang, F. Hafid, A global–local approach to predict the fretting-fatigue failure of clamped aluminum powerline conductors: From mono-contact crossed wires to full conductor vibrational tests, Engineering Failure Analysis 146 (2023) 107073 (https://doi.org/10.1016/j.engfailanal.2023.107073)

A global-local approach to predict the fretting-fatigue failure of clamped aluminum powerline conductors: from mono-contact crossed wires to full conductor vibrational tests

Julien Said[a,b,d], Siegfried Fouvry[a], Georges Cailletaud[b], Stéphanie Basseville[b], Marc Coulangeon[c], Jérôme Brocard[c] ,Christine Yang[d], Fikri Hafid[d]

[a] Ecole Centrale de Lyon, UDL Univ. De Lyon, LTDS-CNRS 5513, 36 Avenue Guy de Collongue, 69134 Ecullye France

[b] MINES ParisTech, PSL Research University, MAT-Centre des Matériaux, CNRS UMR 7633, BP87, 91003, Evry, France

[c] DERVAUX, ZI Le Bec, Allée Ampère, 42500 Le Chambon-Feugerolles, France

[d] RTE – Direction de la R&D – Pôle Smartlab, 92073, Paris la Defense Cedex, France

Key words: Fretting-fatigue; stress gradient; critical distance method, aluminum; failure analysis

Abstract
This work focuses on a multiscale analysis of the fretting-fatigue endurance of aluminum strands within overhead conductors. Based on experimental results, Crossland, Fatemi Socie and SWT fatigue criteria were applied using a Finite Element Method (FEM) modeling. These were used with the critical distance method calibrated on the fretting-fatigue failure of crossed mono-contact strands. With this strategy, the SWT criterion gave the best lifetime estimates as well as the shorter critical distance. By conducting a stress gradient analysis, it is concluded that the shorter the critical distance, the better the contact stress description and finally the better the prediction. This optimized critical distance – stress gradient strategy is then transposed to the complete 3D simulation of a complete multi-strand cable structure subjected to vibrational bending loadings. The comparison with real structural tests confirms the capacity of the proposal to estimate the fretting-fatigue risk.

1. Introduction

Power grids are designed to be operated for long periods of time, and are naturally subjected to various causes of degradation. Thus, a better understanding of the aging mechanisms of their components, such as conductors of overhead powerlines (Fig. 1a), stands as a major challenge. It may help the Transmission System Operator (TSO) to adapt power grids maintenance, repair protocols and reduce the associated costs. In this context, the presented work focuses on the mechanical damage occurring at the contacts existing within the conductor.

The specific type of conductor studied here is an Aluminum Conductor Steel Reinforced (ACSR) assembly consisting of a core and two inner layers of steel strands, and two outer layers of aluminum strands (Fig. 1b). Because of its wire rope structure, this kind of assembly induces a lot of contacts between its strands. When the wind induces aeolian vibrations on the conductor, it may cause small oscillatory movements within these contacts, which are defined as fretting. This tribological loading can nucleate cracks that can then be propagated by fatigue bulk stress. In that case, the associated damage process is called fretting-fatigue which is the main topic of this work.

Fretting-fatigue is known to reduce the total lifetime of conductors, with damage especially located in the clamping zone [1]–[8]. This area makes the link between a power line and an electric pylon, and is the critical region for fretting-fatigue failures on aluminum strands (Fig. 1c and 1d).

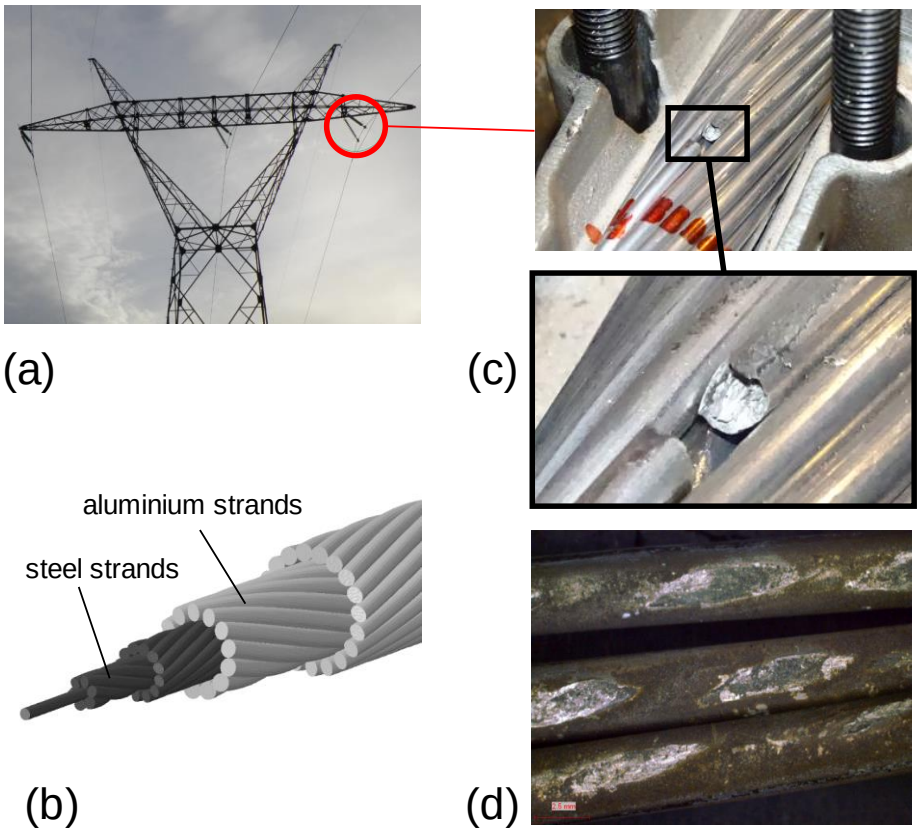

Fig. 1: (a) Electric pylon supporting three overhead conductors; (b) 3D view of the studied ACSR; (c) close-up view of a conductor in the clamping zone, displaying an external layer failure; (d) potential fretting scars on the outer layer in the clamping area.

In that sense, being able to predict the fretting-fatigue lifetime associated with a single contact between two strands in this clamping zone is a key issue. This topic remains of great interest in the academic community as many recent work keep addressing fretting-fatigue applied to overhead conductors [9]–[12]. Previous studies have also been conducted to model the conductor-clamp assembly in order to assess realistic fretting-fatigue loading conditions and then use these data as input for a single contact model [13]. A common strategy to evaluate the lifespan associated with such a configuration is to use multiaxial fatigue criteria to predict the crack nucleation, with the hypothesis that the residual number of cycles to failure after nucleation is negligible. Furthermore, due to the high stress gradients induced by a fretting contact, fatigue criteria cannot be applied directly on the surface and a nonlocal method has to be considered [14]–[20]. Process volume stress averaging strategy [14], [15], or equivalent critical distance method could be considered [17]. The chosen approach in this work is the critical distance method, which is often used for similar problems in fretting or fretting-fatigue. Hence, its reliability depends on the choice of the critical distance noted l_C. In that matter, some authors consider a material dependent parameter such as the microstructural grain size [16], [21], while Taylor [19] proposed to link l_C to the short-to-long crack transition distance b_0. Considering the Kitagawa-Takahashi formalism [22], the critical distance would be given by the relation $l_C = b_0/2$ [17], [19], [20].

Another classical approach consists in calibrating an optimal critical distance from plain fretting experiments [13] to predict the incipient crack formation then to integrate the crack propagation stage to establish the fretting-fatigue endurance [23]. This more comprehensive methodology gives interesting results and insights about the behavior of cracks within the studied aluminum, but is rather long and complex to set up.

The alternative strategy adopted in this work consists in applying a multiaxial fatigue analysis where the optimal critical distance is calibrated using the fretting-fatigue endurance at 10^7 cycles (i.e. failure endurance threshold) of crossed aluminum mono-contacts. This strategy was already adopted in [17], [20], however, the present investigation intends to compare three distinct fatigue criteria considering a 3D fretting-fatigue contact modeling. The Crossland and Smith-Watson-Topper (SWT) have been compared, and for each one of them, a unique critical distance is considered. The goal is to test the consistency and discrepancy of these methods regarding the applied stress gradient conditions. The fretting-fatigue conditions were experimentally applied using a dedicated test bench with two hydraulic actuators, allowing to control the tangential load amplitude Q*, the normal load P and the fatigue loading σ_f separately. From this investigation, an optimized multiaxial fatigue criterion – critical distance combination is deduced which is successively transposed in a complete 3D FEA simulation of multi-strand cable structure enduring vibrational bending loadings to predict the fretting-fatigue damage of Aluminum Conductor Steel Reinforced (ACSR) assembly.

2. Material and experimental setup

2.1. Conductor and aluminum description

Steel strand failures are rarely observed in ACSR conductors which is why only the external aluminum strands are considered in this investigation [24]. For the studied ACSR, the steel strands have a nominal diameter of 2.40 mm while aluminum ones (purity >99%) have a diameter of 3.60 mm. The two outer layers have a different lay angle that results in a relative contact angle $\beta = 30°$ between the strands from these two consecutive layers. Scars associated with this type of contact are illustrated on the figure 1b for an aged ACSR.

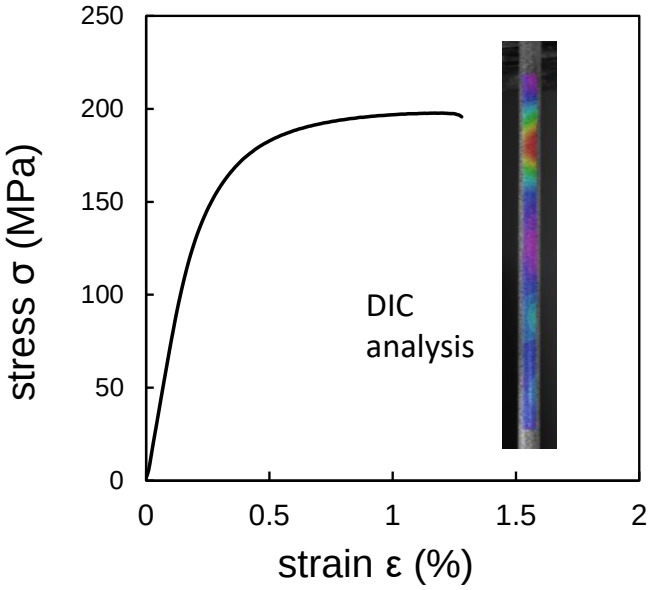

Fig. 2: Studied aluminum *monotonic stress – strain curve obtained through Digial Image Correlation (DIC).*

The monotonic behavior has been characterized through tensile tests on single aluminum strands. To address the "body-necking" phenomenon, the Digital Image Correlation (DIC) technique was used to measure the strain field on the tensile sample. The corresponding stress-strain plot is represented on figure 2, and the mechanical properties deduced from these tests are listed in table 1. In addition to these data, plain fatigue tests were conducted for various loading ratios $R = \sigma_{min}/\sigma_{max}$. The experimental procedure to avoid buckling and early failures is described in [13]. The results obtained for R = -1 and R= 0.2 are plotted in figure 3.

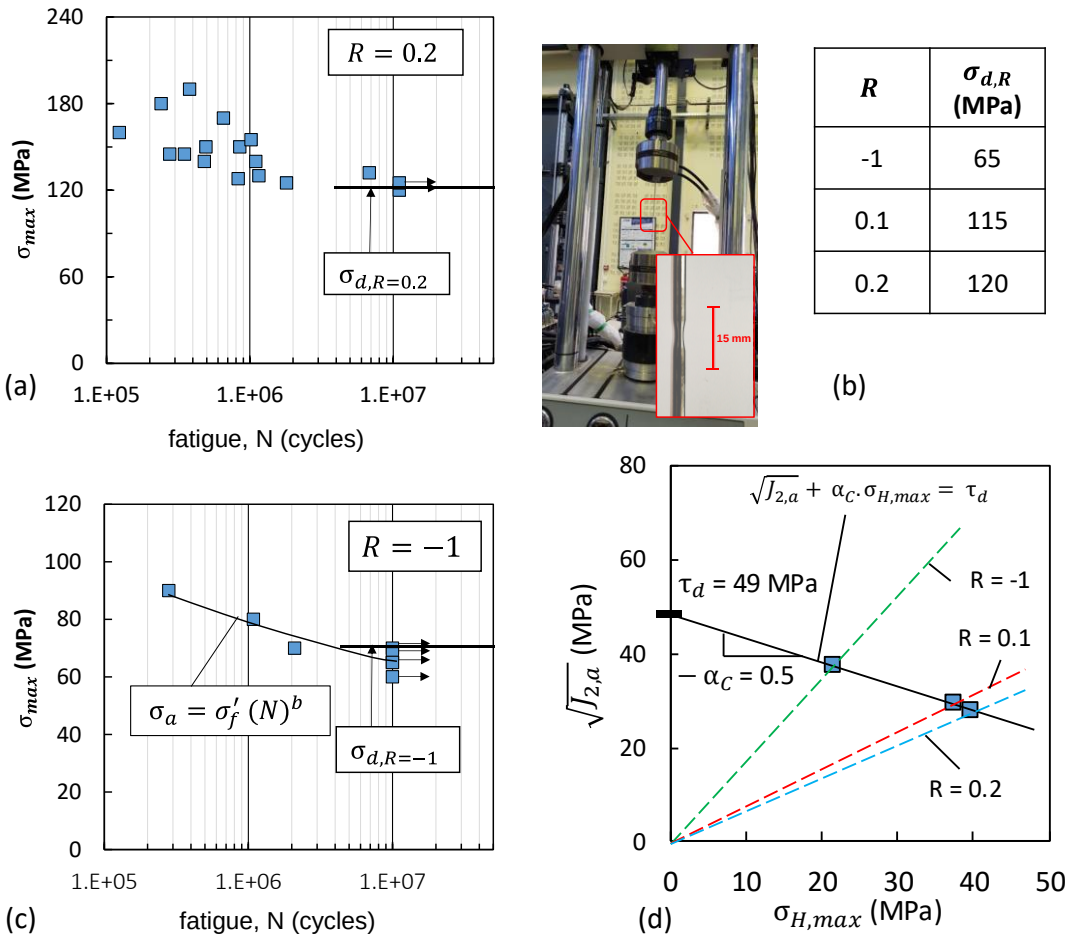

R	$\sigma_{d,R}$ (MPa)
-1	65
0.1	115
0.2	120

Fig. 3: (a,) Wöhler curve for the loading ratio R= 0.2 ; (b) Compilation of the fatigue limits for different stress ratio (R); (c) Identificatin of the Basquin's law of the fatigue endurance curve with R=-1 ; (c) Modified Dang Van diagram used to deduce the torsion fatigue limit τ_d ($\sigma_{d,-1}$ = 65 MPa, $\sigma_{d,0.1}$ = 115 MPa, $\sigma_{d,0.2}$ = 120 MPa

The plain fatigue behavior can be modeled with a power law using the Basquin-Coffin-Manson equation linking the stress amplitude σ_a with the number of cycles to failure N (relation (1)).

$$\frac{\Delta\sigma}{2} = \sigma_a = \sigma'_f (2N)^b + \varepsilon'_f (2N)^c \quad (1)$$

With:

- σ'_f the fatigue strength coefficient
- b the fatigue strength exponent
- ε'_f the fatigue ductility exponent
- c the fatigue ductility exponent

In the current case, studied lifetimes stand between 10^6 and 10^7 cycles. Therefore, assuming the elastic hypothesis, it leads to:

$$\sigma_a = \sigma'_f (2N)^b \quad (2)$$

According to the least square error, σ_f' and b are identified using the data on figure 2b and listed in table 1. Alternatively, shear mechanisms can be quantified in plain fatigue using an analogous power law. The torsion amplitude limit τ_a can also be described by the Basquin's law, so that:

$$\tau_a = \tau'_f (2N)^{b'} \quad (2)$$

With:

- τ'_f the torsion fatigue strength coefficient
- b' the torsion fatigue strength exponent

It is generally considered that b = b', and the torsion fatigue limit can be extrapolated according [25] that:

$$\frac{\sigma_d}{\tau_d} = \frac{\sigma'_f}{\tau'_f} \quad (3)$$

The uniaxial fatigue limit at R = -1 is directly extracted from the plain fatigue data displayed in figure 2b, giving σ_d = 65 MPa for the limit lifetime 10^7 cycles to failure. Finally, the torsion fatigue limit has previously been extrapolated using a modified Dang Van diagram, as detailed in [13] and represented in figure 3. This plot relies on the Crossland formalism described in section 4.3. In addition to the fatigue limit (at 10^7 cycles) σ_d for R = -1, two other limits were assessed for R = 0.1 and R = 0.2. These plain fatigue tests gave $\sigma_{d,0.1}$ = 115 MPa and $\sigma_{d,0.2}$ = 120 MPa, respectively. These three limits can be placed in the ($\sigma_{H,max}$; $\sqrt{J_{2,a}}$) plane and belong to the fracture border defined by the equality of eq. (8). As this border is linear, the torsion fatigue limit can be directly extrapolated and corresponds to $\sqrt{J_{2,a}}$ when the hydrostatic pressure $\sigma_{H,max}$ is equal to zero. This leads to τ_d = 49 MPa for 10^7 cycles to failure, and the deduced value for τ_f' is shown in table 1.

Table 1: List of material parameters used to describe the aluminum elastic behavior

E (GPa)	ν	C	σ_{UTS} (MPa)	$\sigma_{d(-1)}$ (MPa)	$\tau_{d(-1)}$ (MPa)	σ'_f (MPa)	b	τ'_f (MPa)	b'
68	0.34	160	200	65	49	274.45	-0.086	206.9	-0.086

2.2. Identification of the plastic behavior

Cyclic tensile and compressive tests have been conducted to gather data about the cyclic hardening (Bauschinger effect) of the material (figure 4). Based on these tests, a material law

with combined non-linear kinematic and isotropic hardening has been identified. Using the Von Mises formalism, the yield function associated with such a law has the following form:

$$f\left(\underline{\underline{\sigma}}\right) = J\left(\underline{\underline{\sigma}} - \underline{\underline{X}}\right) - \sigma_Y - R(p) \quad (4)$$

With:

- J the Von Mises scalar norm. The Von Mises equivalent stress σ_{VM} corresponds to $\sigma_{VM} = J(\underline{\underline{\sigma}})$
- $\underline{\underline{X}}$ the kinetic hardening tensor variable
- R the isotropic hardening variable
- p the plastic variable defined as the norm of the plastic strain ε_p: $\underline{\underline{\varepsilon_p}} = p\,\underline{\underline{n}}$, where $\underline{\underline{n}}$ is the flow direction tensor.

At the first order, this material law can be fully described with 4 coefficients C, D, Q and a listed in table 2. The hardening variables are then defined through the following differential equations:

$$\dot{\underline{\underline{X}}} = \frac{2}{3} C \dot{\underline{\underline{\varepsilon}}}_p - D\,\underline{\underline{X}}\,\dot{p} \quad (5)$$

$$\dot{R} = a(Q - R)\dot{p} \text{ or } = Q(1 - e^{-ap}) \quad (6)$$

The correlation between experiments and the given cyclic plastic law is rather good, which indirectly supports the proposal to describe the plastic behavior of the studied aluminum.

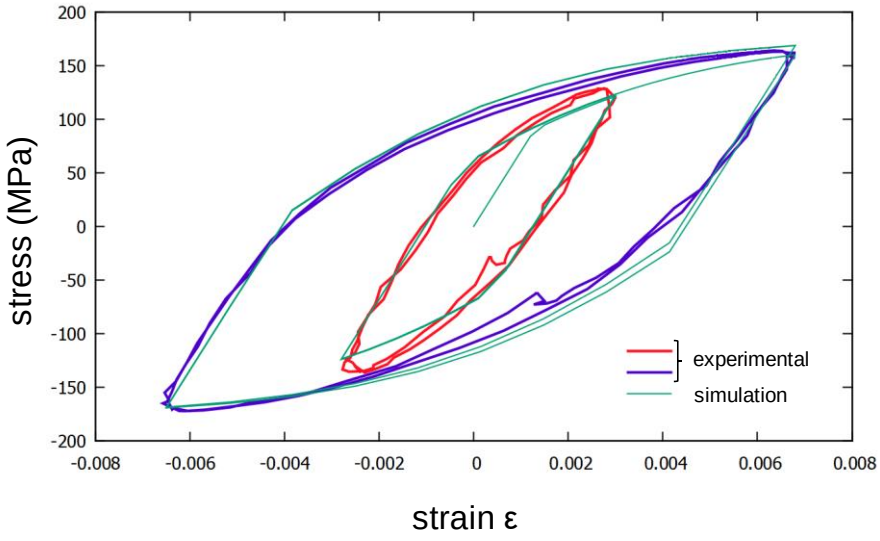

Fig. 4: Comparison between experimental and simulated stress-strain hardening cycles

Table 2: Hardening parameters used to describe the plastic law identified through the stress – strain loops on figure 4

C (MPa)	D	Q (MPa)	a
5000	500	10	200

2.3. Fretting-fatigue rig and contact configuration

The fretting-fatigue rig used for this work is represented in figure 5a. It uses two distinct hydraulic actuators and two samples, and reproduces one single contact between two aluminum strands from the outer layers of an ACSR. The lower actuator is force controlled, and applies the fatigue loading $\sigma_f(t)$ on the vertical fatigue sample (Fig. 5b and 5c). The fretting sample (Fig. 5c) consists in a smaller strand contacting the fatigue sample with a relative angle $\beta = 30°$. It is moved by the upper actuator, and applies the relative displacement $\delta(t)$ in the fretting contact. It is this displacement that induces the tangential force Q(t), measured using two force sensors located at each end of the fatigue sample. The difference between the two measured forces is noted $Q_{diff}(t)$, and is equal to zero if there is no contact. In addition to the aluminum/aluminum contact, a PTFE polymer counter face is added to counterbalance the applied normal load preventing in turn the bending of the fatigue sample. This counter body has been chosen because of its low friction coefficient $\mu_{PTFE/al}$, in order to reduce its tangential contribution compared to the aluminum/aluminum contact. The value of $\mu_{PTFE/al}$ has been deduced from preliminary variable displacement tests as described by Voisin [26], giving $\mu_{PTFE/al} = 0.04$. The actual tangential load amplitude Q* corresponding to the aluminum/aluminum contact is then obtained through equation (7). In this equation, P is the fretting normal force, and is kept constant throughout every test. The frequency is systematically set to 20 Hz, and the limit number of cycles tested is 10^7 cycles.

$$Q^* = Q^*_{diff} - \mu_{PTFE/al}.P \quad (7)$$

Using this procedure, various experiments were performed to establish the friction coefficient at the sliding transition between partial and gross slip which was estimated around $\mu = 1.1$. Note that this value was assumed representative of the friction coefficient operating in sliding zones of the partial slip contact and therefore will be considered in the following simulations.

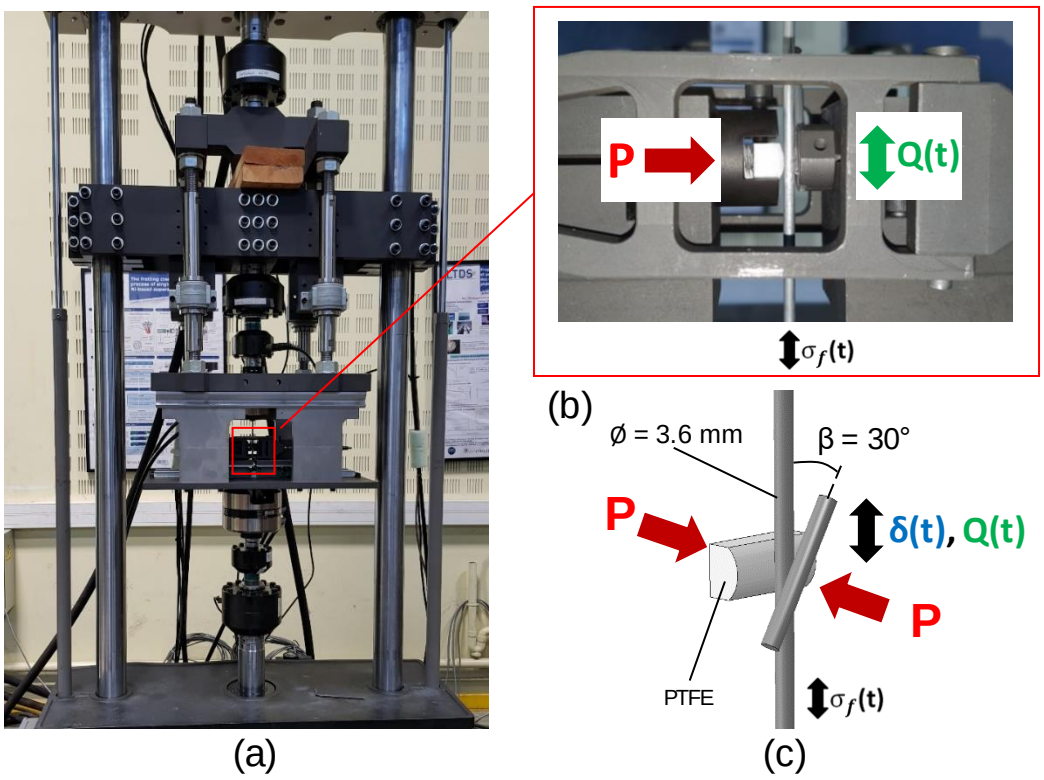

Fig. 5: (a) View of the double actuator fretting-fatigue rig; (b) close up view of the contact zone; (c) schematic representation of the contact zone.

3. Experimental results

3.1. Fretting-Fatigue results

A key aspect for any fretting-fatigue damage prediction is to establish the representative loading conditions applied to the studied assembly. Knowing these loading and boundary conditions, the studied material could be investigated properly thus to establish relevant damage laws. Former numerical investigations suggest that the most critical fretting fatigue loadings occurring between crossed aluminum wires in clamped conductors [13] are systematically related to partial slip conditions where $50 < P < 300$ N with $\sigma_{f,max} > 30$ MPa. Considering these numerical conclusions, the applied the fretting-fatigue conditions have been chosen in order to get as many failures as possible. More severe loadings would induce early breaks located at the jaws of the bench, while less damaging ones would not warranty any failure before 10^7 cycles. Three series of tests have been performed:

- Variable fatigue (Fig. 6a): a set of tests with variable fatigue loadings and constant fretting conditions (Fig. 6a). The fretting forces have been set to P = 200 N and Q* = ± 200 N. The loading ratio $R = \sigma_{min}/\sigma_{max}$ is kept the same with R = 0.5 for all tests, and the corresponding lifetimes are plotted versus the maximum stress σ_{max}.

- Variable tangential force amplitude (Fig. 6b): a set of tests with variable tangential force amplitude Q* with constant normal force P and fatigue stress $\sigma_{f,max}$ (Fig. 6b). While the former is set to P = 200 N, the latter is applied in order to have σ_{max} = 70 MPa and R = 0.5.

- Variable normal force (Fig. 6c): the last set of data has already been shown and studied in the previous work about quantifying the propagation mechanisms (Fig. 6c) [23]. Those tests were conducted to highlight the influence of the normal force P on the fretting-fatigue life, with a sharp increase when P exceeds a given threshold. Some of these results were reused in this work to complete the previous data. The tangential force amplitude Q* was kept at Q* = ± 150 N, with σ_{max} = 70 MPa and R = 0.5.

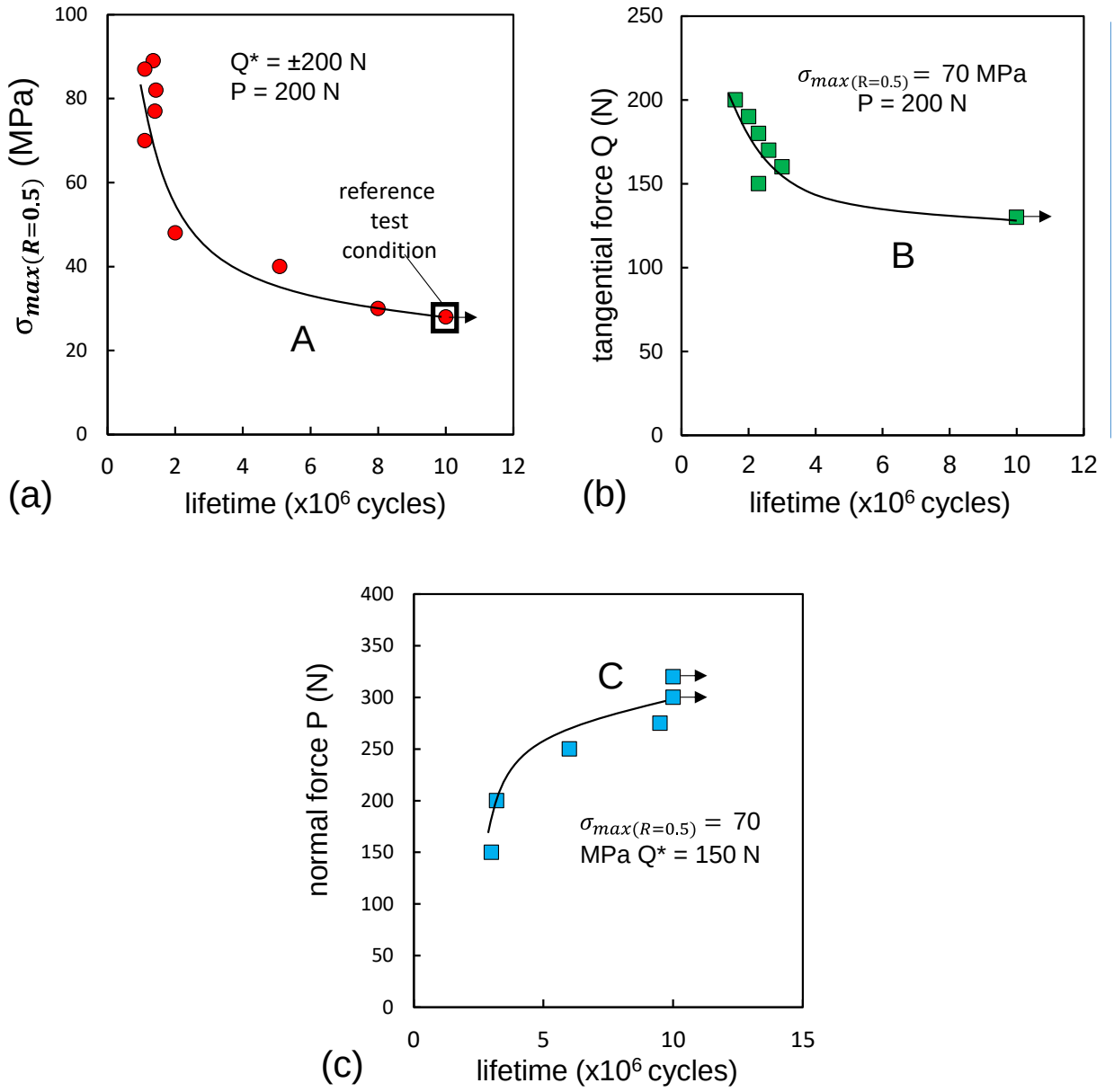

Fig. 6: (a) Wöhler curve for Q = ± 200 N, P = 200 N, R = 0.5 and variable fatigue loading; (b) Wöhler curve for P = 200 N, $\sigma_{f,max}$ = 70 MPa, R = 0.5 and variable tangential force amplitude Q*; (c) Wöhler curve for Q* = ± 150 N, σ_{max} = 70 MPa, R = 0.5 and variable normal force P.*

Among these experimental results, a set of loading conditions have been selected in order to be simulated using a numerical Finite Element Method (FEM) model, as described in the following section. All these loading conditions are marked using (**) in table 3.

Table 3: List of the fretting-fatigue conditions tested experimentally, with simulated cases marked by (**); N_C, N_{SWT} and N_{FS} are the predicted lifetimes according to the Crossland, SWT and FS criteria, respectively (for a crossed aluminum strand contact, strand diameter Ø = 3.6 mm and relative angle β = 30°)

Test number	**tangential load Q* (N)**	**normal load P (N)**	**σ_{max} R = 0.5 (MPa)**	**experimental lifetime ($\times 10^7$ cycles)**	**N_C ($\times 10^7$ cycles)**	**N_{SWT} ($\times 10^7$ cycles)**	**N_{FS} ($\times 10^7$ cycles)**
A_1 (**)	**200**	**200**	**28**	**=10**	**10**	**10**	**10**
A_2 (**)	200	200	30	8	9.9	11	10
A_3 (**)	200	200	40	5.09	6.5	5	6.6
A_4 (**)	200	200	48	2	5.2	0.97	5.3
A_4 (**)	200	200	70	1.1	3.24	0.18	3.3
A_5 (**)	200	200	78	1.4	2.9	0.14	3.0
A_6	200	200	82	1.43			
A_7	200	200	87	1.1			
A_8	200	200	89	1.35			
B_1 (**)	130	200	70	>10	>10	>10	>10
B_2 (**)	150	200	70	3.2	>10	3.2	10
B_3 (**)	160	200	70	3	>10	2.87	4.9
B_4	170	200	70	2.6			
B_5 (**)	180	200	70	2.3	1.7	0.4	1
B_6	190	200	70	2			
C_1 (**)	150	150	70	3	9.5	0.41	>10
C_2 (**)	150	250	70	6	>10	7.9	>10
C_3	150	275	70	9.5			
C_4 (**)	150	300	70	>10	>10	9.7	>10
C_5	150	320	70	>10			

To calibrate the non-local fatigue analysis and identify a relevant critical distance a reference loading case corresponding to the limit lifetime 10^7 cycles was chosen on the variable fatigue endurance curve (Fig. 6a): A1 Q* = ± 200 N, P = 200 N, σ_{max} = 28 MPa and R = 0.5.

3.2. Fracture analysis

3.2.1. Unfailed specimens

All fretting-fatigue tests were stopped at 10 million cycles when the fatigue sample would not break. In that case, the corresponding strands would be post-processed with polishing and optical microscopy. Typical crack geometries are displayed in figure 7, with an illustration of a crack observed in fretting-fatigue (for the reference case defined in the previous section) in figure 7a and in plain fretting (Q* = ± 150 N, P = 200 N and N = 300 000 cycles) in figure 7b. These views can be also used to define the propagation angle noted θ, corresponding to the angle between the crack plane and the normal axis to the surface (z direction). Crack nucleation occurs at the contact edges with a slant crack angle, θ_{exp} = 60° without showing any successive bifurcation.

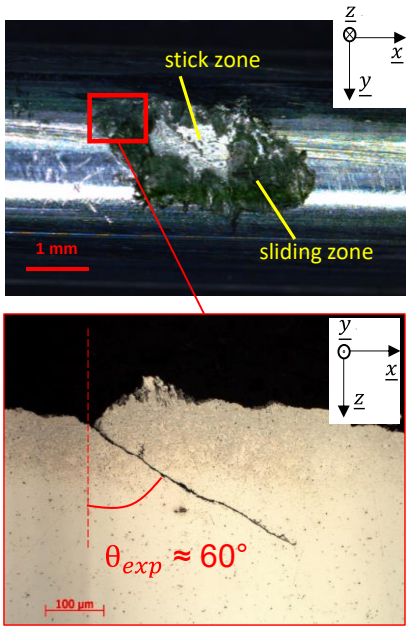

Fig. 7: (a) Fretting Fatigue cracking: optical view of the fretting scar with a close-up cross-sectional view of the nucleated crack at the edge of the contact (Q = ± 150 N, P = 300 N, $\sigma_{f,max}$ = 70 MPa, R = 0.5, N > 10^7 cycles).*

3.2.2. Failed samples

Figures 8 and 9 support the analysis conducted on a failed sample, corresponding to the conditions labeled B_2 in table 3 (Q* = ± 150 N, P = 200 N, $\sigma_{f,max}$ = 70 MPa, R = 0.5 and N = 3.2 million cycles). On figure 8a, it can be seen that the crack started from the edge of the contact and propagated until total failure. The last analysis performed is illustrated in figure 9, with pictures obtained through Scanning Electron Microscopy (SEM). The overall view of the strand surface is shown in figure 8b, seen from the A – A plane defined in figure 8a. On this fracture surface, four morphologies can be distinguished (figure 8c):

- Region (1): Immediately below the fretting contact, small steps and ridges are visible in the region that has been subjected to both fatigue stress and strong fretting stress. These

chaotic features may result from friction between the crack lips and the associated plastic effects on the surface.

- Region (2): This area is characterized by mixed features, with both smooth planes and rough zones. As it is further away from the contact, these shapes may be linked to plain fatigue conditions. They can also be related to friction effects between the crack lips. This region stands as the intermediate stage between the initiation (region 1) and the last stage before failure (region 3).

- Region (3): This region most likely corresponds to the last stage of fatigue propagation before reaching the total failure. The surface is very smooth, with almost no clear features but some asperities. Similar morphologies can be observed for cracks propagated in plain fatigue for other ductile materials, with occasionally additional ridges from the successive advances of the crack.

- Region (4): Dimples resulting from microvoid coalescence can be seen in the lower part of the fracture surface. These features are usually related to catastrophic failures on ductile materials. Hence, this region corresponds to time of failure of the strand.

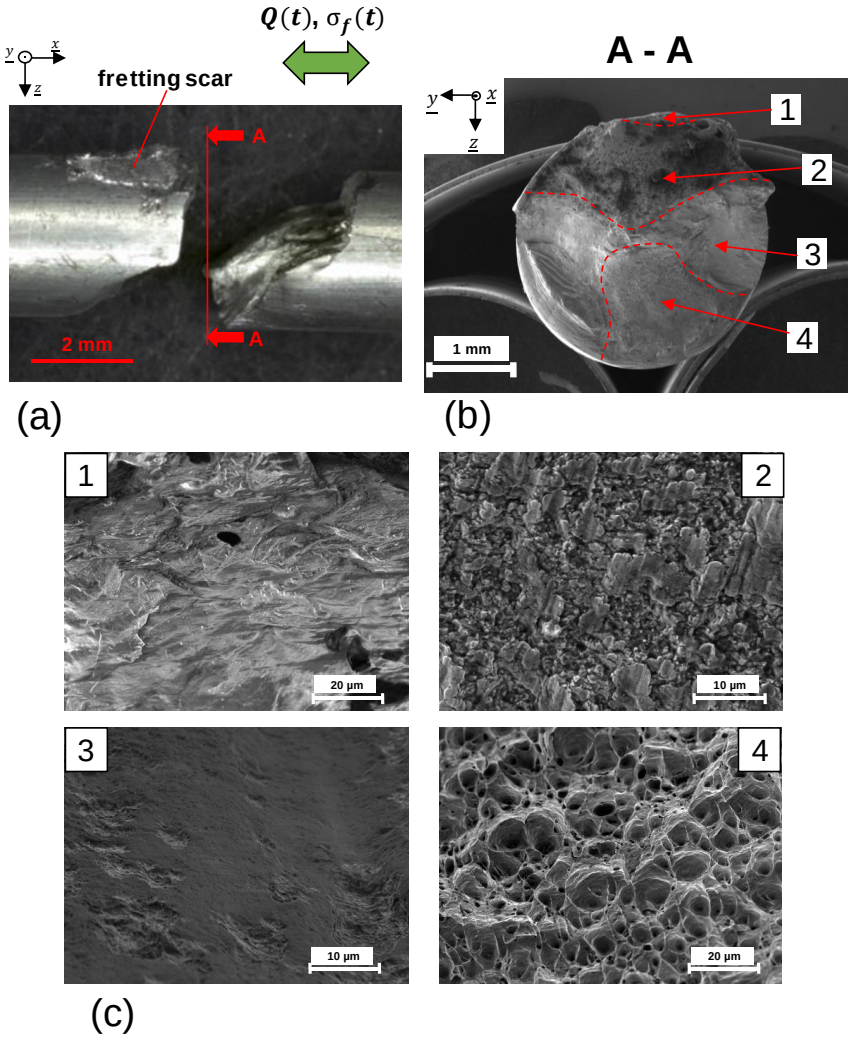

Fig. 8: (a) Optical view of the failure zone of a strand loaded in fretting-fatigue (Q = ± 150 N, P = 200 N, $\sigma_{f,max}$ = 70 MPa, R = 0.5, N =3.2 million cycles); (b) SEM front view of the fracture surface, with four regions delimited; (c) SEM close-up view of the highlighted regions and associated morphologies.*

In addition to these front observations, a particular attention has been given to the various orientations on the fracture surface. Using a numerical microscope, the medium profile of the fracture surface is displayed in figure 9b. On this view, two major slopes can be seen. Right below the contact, a "plateau" characterized by a rather low slope can be seen and corresponds to region (2) in figure 8. This plateau is also clearly visible on figure 9a on the upper left part of the view. Then, the slope sharply increases until the other face of the sample, and corresponds to regions (3) and (4).

Figures 9c, 9d and 9e focus on the plateau to get additional data on this area. Because of its low slope, it is suitable with more accurate profilometry. An interferometer microscope has been used on the region highlighted in figure 9c and covers regions (1) and (2). This closer view allows to

quantify the initial angle of the nucleated crack right under the contact surface (region (1)), as well as the bifurcation occurring in region (2). The associated profile is plotted in figure 9e. The major conclusion arising from these figures is that a clear bifurcation occurs between regions (1) and (2) that can't be seen on optical observations on unfailed samples. During the nucleation stage, the crack angle $\theta_{exp,1} = 55°$ is consistent with the angle $\theta_{exp} = 60°$ measured on unfailed samples (Fig. 7), with the promotion of shear mechanisms. However, beyond 200 µm, the crack path changes orientation to display a lower angle $\theta_{exp,2} = 15°$. It then becomes more sensitive to the mode I principal stress σ_I, which is the plain fatigue main mechanism. Finally, during the last stage of propagation, above 1.8 mm extension, the crack bifurcates again leading to larger angle of propagation $\theta_{exp,3} \approx 60°$.

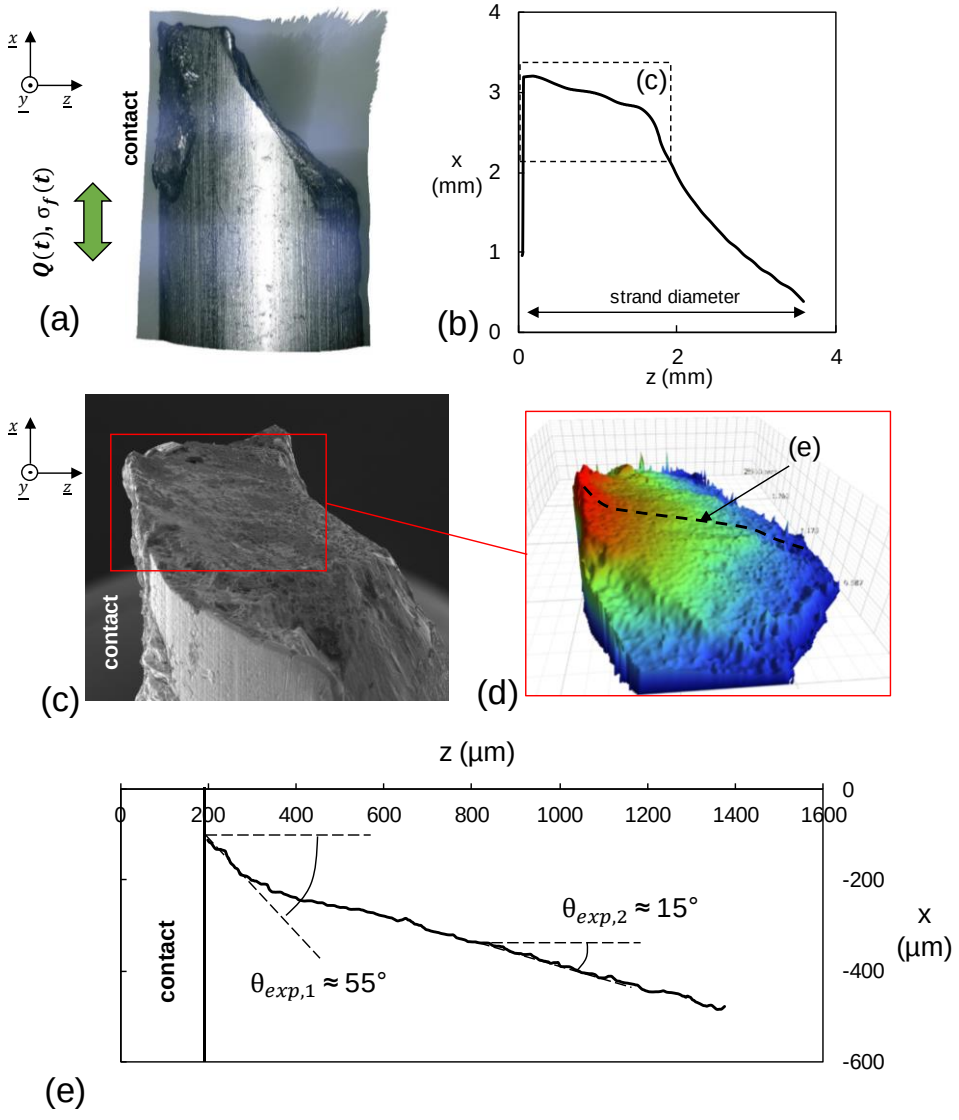

Fig. 9: (a) Side view of the strand failed in fretting-fatigue (Q = ± 150 N, P = 200 N, $\sigma_{f,max}$ = 70 MPa, R = 0.5, N =3.2 million cycles); (b) linear height profile of the strand along its diameter and starting from the contact zone; (c) SEM view of the tilted sample, focusing on the first stage*

of propagation; (d) 3D profile of the fracture surface close to the contact area; (e) linear height profile measured in the area visualized in (d).

4. Finite Element Modeling of crossed mono-contact configuration

Extensive numerical studies based the Finite Element Method (FEM) have been conducted to capitalize on the experimental work described earlier and return actual predictions regarding the lifetime to failure of such contacts. This section describes the adopted methodology, the three multiaxial fatigue criteria that have been used and the discussion regarding their respective performances.

4.1. Model description

The 3D modeling of a single contact between two aluminum strands consists in two 5 mm long half-cylinders with a 3.6 mm diameter in contact, as illustrated in figure 10. This model is suited with the ABAQUS/Standard implicit solver associated with the elastic hypothesis, and uses linear hexahedral elements C3D8. All stresses are computed at the integration points within these elements. The mesh is refined in the contact zone with a minimum typical length scale of 25 µm. Because of their low curvature compared with the size of the model, both strands are considered as straight cylinders, their helical shape is then neglected. The normal force P is applied on the upper strand as well as the tangential load Q through reference points coupled with this upper part. The fatigue bulk stress σ_f is applied as a negative surface pressure on the end of the same strand. The contact interaction is modeled with the penalty algorithm, and for each simulation three distinct steps are described.

- Step (1): Instead of directly applying the targeted normal force at the beginning of the simulation, a very small displacement is firstly applied. This preliminary step ensures the stability of the contact algorithm and the convergence of the next steps.

- Step (2): The normal force P is fully applied to the upper strand through a ramp amplitude. In the meantime, the mean value for the fatigue bulk stress is also applied.

- Step (3): once the contact is loaded, both the tangential load and the fatigue stress are imposed in phase through a sinusoidal amplitude

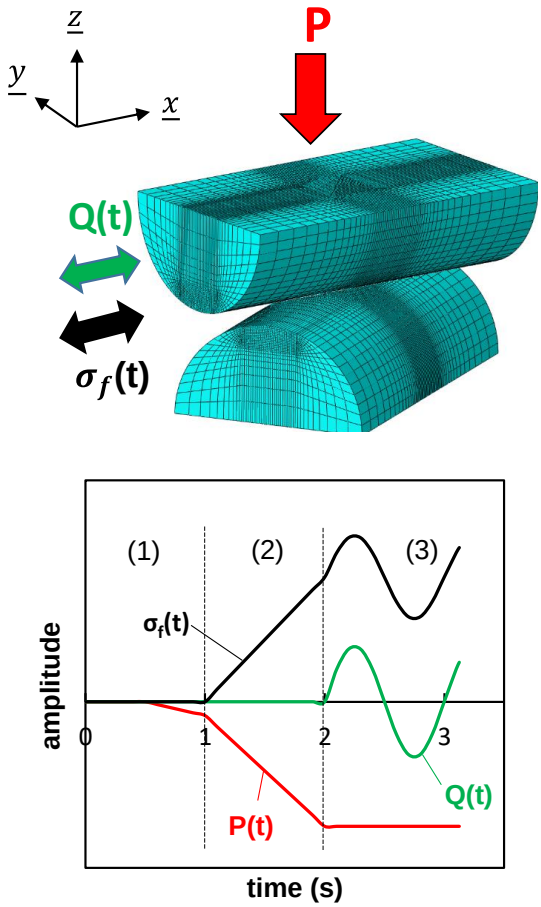

Fig. 10: 3D view of the numerical model used for the aluminum/aluminum contact and the loading sequence used for every fretting-fatigue simulation.

All the material parameters used for the simulations were experimentally identified. The material is considered isotropic, with a Young's modulus E = 65 GPa and a Poisson ratio ν = 0.34.

4.2. Discussion regarding the elastic hypothesis

The reference case condition (Q* = ± 200 N, P = 200 N, $\sigma_{f,max}$ = 28 MPa and R = 0.5) was first simulated using an elastic assumption. The Von Mises profile at the vertical axis of the trailing contact border (i.e. Hot Spot tensile stress position), is displayed in figure 11. Elastic computations lead to a very sharp discontinuity leading to a nonrealistic 750 MPa value on the top surface. From this analysis it could be concluded that elastoplastic simulations are systematically required to evaluate the effect of plasticity, a similar simulation has been performed applying the non-linear kinematic and isotropic hardening law of the studied material. The corresponding Von Mises profiles extracted at the elastic shakedown state (i.e. after 50 numerical cycles) are compared. As expected smaller and more realistic Von Mises stresses

reaching 200 MPa on the top surface due to the hardening process are observed. However, below a threshold subsurface position $z > z_p = 200$ µm, both elastic and plastic profiles are converging with a relative error remaining under 15%. Hence, assuming that the optimal critical distance used for predicting the fretting-fatigue cracking risk is longer than z_p (ie. $l_C > z_p$), it could be concluded that an elastic hypothesis can reasonably be adopted. Hence, an elastic hypothesis is considered for following fatigue stress analysis such that the $l_C > z_p$ condition is satisfied. Note that this z_p - l_C correlation indirectly justifies former research studies showing good prediction of the fretting-fatigue risk using nonlocal elastic fatigue stress analysis although surface plasticity was implicitly occurring [15].

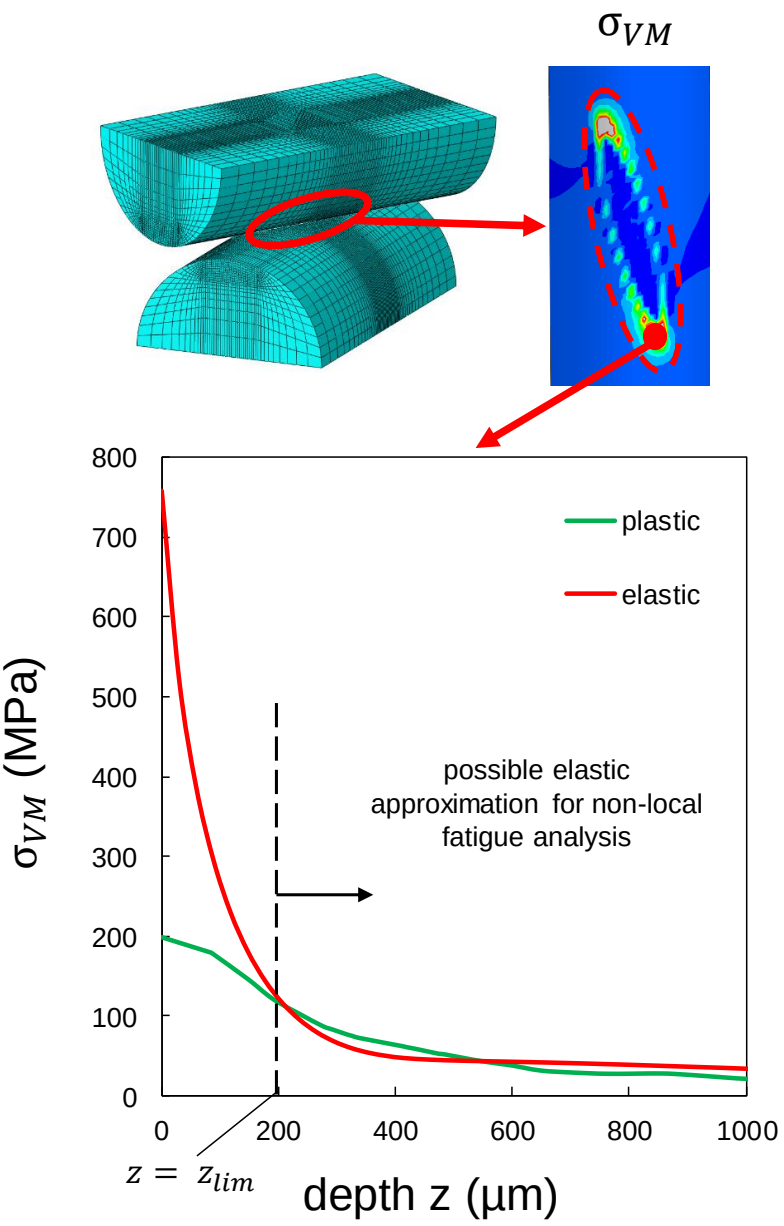

Fig. 11: Evolution of the Von Mises equivalent stress σ_{VM} versus the depth below the hotspot at Q(t) = +Q, comparison between fully elastic and plastic modeling (reference case: Q* = ± 200 N, P = 200 N, $\sigma_{f,max}$ = 28 MPa, R = 0.5).*

4.3. Multiaxial fatigue criteria

4.3.1. Crossland criterion

The Crossland multiaxial fatigue criterion has an invariant-based formulation focused on the shear damage suffered by the material. The nucleation (or failure) condition is given by:

$$\sigma_C = \sqrt{J_{2,a}} + \alpha_C . \sigma_{H,max} > \tau_d \quad (8)$$

with:

$$\alpha_C = \frac{\tau_d - \sigma_d/\sqrt{3}}{\sigma_d/\sqrt{3}} \quad (9)$$

In this work, the α_C parameter was computed from fatigue limit conditions and was assumed constant whatever the endurance range (N). Considering the fatigue limits defined in section 2.1, it was found that $\alpha_C = 0.3$.

In eq. (8) and (9), $J_{2,a}$ is the second invariant of the deviatoric stress amplitude tensor and $\sigma_{H,max}$ the maximum hydrostatic stress during a loading cycle. When the condition (8) is fulfilled, the nucleation or failure is expected to occur before 10^7 cycles. This formulation can also be extrapolated to link the equivalent Crossland stress σ_C to the number of cycles to failure by combining eq. (2) and eq. (8):

$$\sigma_C = \sqrt{J_{2,a}} + \alpha_C . \sigma_{H,max} = \tau_f' (2N)^{b'} \quad (10)$$

4.3.2. The Fatemi-Socie (FS) criterion

The invariant-based Crossland criterion is fast to compute, but does not give any information about crack orientation. The Fatemi-Socie (FS) criterion relies on critical plane analysis based on shear strain damage. Its parameter Γ_{FS} involves the maximum shear strain range $\Delta\gamma_{max}$ and the maximum tensile stress $\sigma_{n,max}$ compared to the σ_Y yield stress of the material.

$$\Gamma_{FS} = \frac{\Delta\gamma_{max}}{2}\left(1 + k\frac{\sigma_{n,max}}{\sigma_Y}\right) \quad (11)$$

The methodology consists in computing this parameter on every integration point, and for each point in all planes along all directions. The crack nucleation is expected to happen in the plane that maximizes Γ_{FS} ; this is the so-called critical plane related to the maximum Γ_{FS} value.

In eq. (16), *k* is an additional material-dependent constant that needs to be determined. The Γ_{FS} is also linked to the lifetime N through a Basquin-based equation that can be written according to the elastic hypothesis as follows:

$$\Gamma_{FS} = \frac{\tau_f'}{G} (2N)^{b'} \quad (12)$$

With G being the shear modulus:

$$G = \frac{E}{2(1+\nu)} \quad (13)$$

As E and ν are already identified, all parameters required to apply the FS criterion are known but the coefficient *k*. Concerning this point, it can be found in the literature [27], [28] that the ratio σ_Y/k is very close to the fatigue strength coefficient σ_f'. With this approximation, the remaining material parameters can be determined, giving G = 25.6 GPa and $k = 0.43$.

4.3.3. The Smith-Watson-Topper (SWT) criterion

The Smith-Watson-Topper (SWT) criterion is also a critical plane approach although it is based on the maximal opening stress $\sigma_{n,max}$ and the associated strain amplitude $\varepsilon_a = \Delta\varepsilon_n/2$. Its parameter is defined as follows:

$$\Gamma_{SWT} = \sigma_{n,max}.\varepsilon_a \quad (14)$$

Like for the FS analysis, this parameter has to be tested on every integration point, and for each point in all planes along all directions. Again, the crack nucleation is expected to happen in the plane that maximizes Γ_{SWT}; this is the so-called critical plane. As it is based on opening stress and strain, this formulation focuses on mode I mechanisms for the crack initiation. In that sense, it is suited for materials with more fragile behavior such as steel or titanium alloys. Still, it can be applied on the studied aluminum to assess its accuracy in this specific configuration.

The SWT parameter can be directly related to the number of cycles to failure N by application of the Basquin's law as expressed in eq. (2) as well as the uniaxial Hooke's law, giving eq. (12):

$$\Gamma_{SWT} = \sigma_{n,max}.\varepsilon_a = \frac{\left(\sigma_f'\right)^2}{E}(2N)^{2b} \quad (15)$$

This formulation is consistent with the elastic hypothesis, as the plasticity contribution is here neglected. Finally, it is possible to express an equivalent SWT scalar stress σ_{SWT} based on Γ_{SWT} as follows:

$$\sigma_{SWT} = \sqrt{E.\Gamma_{SWT}} \quad (16)$$

This stress can directly be compared to the uniaxial fatigue limit σ_d. If $\sigma_{SWT} > \sigma_d$ in any location, then the nucleation/failure is expected to occur before 10^7 cycles.

5. Non local critical distance analysis of experiments: comparison between multiaxial fatigue criterion

5.1 Calibration of the critical distances.

As illustrated in figure 12, the estimation of the critical distances related to Crossland, SWT and Fatemi Socie criteria consists in post processing the reference test endurance condition (Q* = ± 200 N, P = 200 N, $\sigma_{f,max}$ = 28 MPa and R = 0.5). First, the surface distributions of the criteria are computed to estimate the position of the corresponding hot spots (*i.e.* where the maximum value of the fatigue criteria is operating). Then, the subsurface profiles below the latter are established. The related critical distances are then extracted by intersecting the corresponding threshold endurance values. The Crossland analysis consists in comparing the alternated torsion fatigue limit so that:

$$\sigma_C\left(z = l_{C,C}\right) = \tau_{d(-1)} \quad (17)$$

For the Fatemi-Socie criterion, the post processing analysis was arbitrary defined by comparing the Fatemi-Socie (Eq. 17) at 10^7 cycles (i.e. $\Gamma_{FS,10^7} = 1.9\text{x}10 - 3$)

$$\Gamma_{FS}\left(z = l_{C,FS}\right) = \Gamma_{FS,10^7} \quad (18)$$

For the SWT fatigue criterion the correlation is done versus alternated tension-compression fatigue limit:

$$\sigma_{SWT}\left(z = l_{C,SWT}\right) = \sigma_{d(-1)} \quad (19)$$

From this analysis, the following optimal critical distances were found : $l_{C,C}$ = 500µm, $l_{C,FS}$ = 520 µm and $l_{C,SWT}$ = 360 µm.

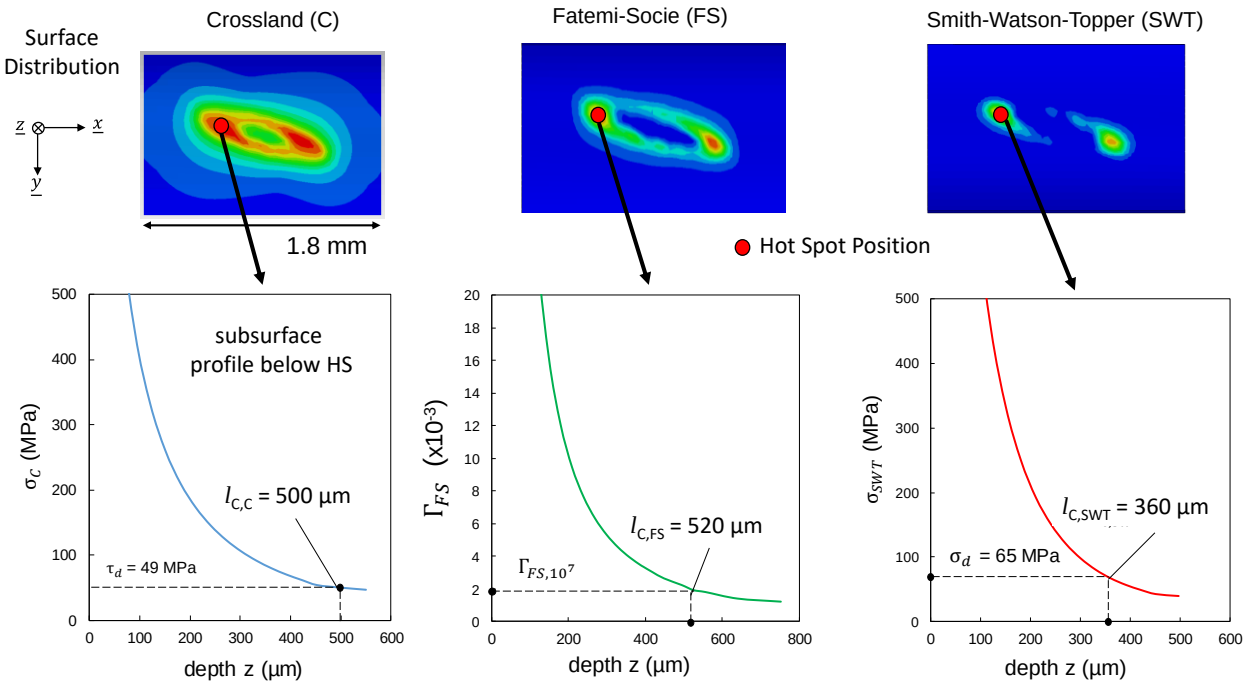

Fig. 12: Identification of the optimal critical distance for the Crossland, Fatemi-Socie and SWT fatigue analysis of the fretting-fatigue experiments applying a post processing analysis of the reference endurance test condition (Q = ± 200 N, P = 200 N, $\sigma_{f,max}$ = 28 MPa and R = 0.5).*

It is interesting to note that the obtained values are significantly longer than z_p = 200 µm which justifies *a posteriori* an elastic stress hypothesis for the fretting-fatigue analysis. Compared with how this calibration is achieved in the literature [16, 29, 30], this application can be considered as a necessary approximation in order to fit with the experimental data with satisfying accuracy.

5.2 Quantitative prediction of the fretting-fatigue endurance using the "optimal" critical distance concept

- *Crossland fatigue criterion*

With the knowledge of $l_{C,C}$, the lifetime to failure N estimated by the Crossland approach can be extrapolated by inverting eq. (10), giving:

$$N_{f,C} = \frac{1}{2}\exp\left(\frac{\ln\left(\frac{\sigma_C(l_{C,C})}{\tau'_f}\right)}{b}\right) \tag{20}$$

Applying eq. (20), the lifetime predictions of experiments marked by (**) in table 3 are computed. The comparison between the predicted and experimental endurances is shown in Figure 13a. Results are divided into two categories highlighted by two distinct colors. The first category is materialized by fully-colored squares, and corresponds to tests with variable fatigue loading with fixed fretting conditions: Q* = ± 200 N and P = 200 N (figure 6a). These conditions are also labeled as A_i in table 3. The second one gathers tests from figure 6b and 6c, *i.e.* tests with fixed fatigue loading $\sigma_{f,max}$ = 70 MPa, R = 0.5 and variable Q* or P (labeled as B_i or C_i in table 3). It can thus be noted that the reference case for which $l_{C,C}$ has been calibrated belongs to the first category. This way of splitting the data highlights the difference of discrepancy in the predictions between tests labeled A_i (variable fatigue) versus B_i (variable tangential force amplitude) or C_i (variable normal force). For the variable fatigue tests, predictions stay within the same order of magnitude, even though they are optimistic and thus non-conservative. For the other set of loadings, the predictions are very dispersive and often predict endurances exceeding 10^7 cycles involving dangerous non conservative assessments. Hence, it appears that the use of the Crossland criterion calibrated on the fretting-fatigue failure and associated with a unique critical distance cannot offer reliable fretting-fatigue failure predictions.

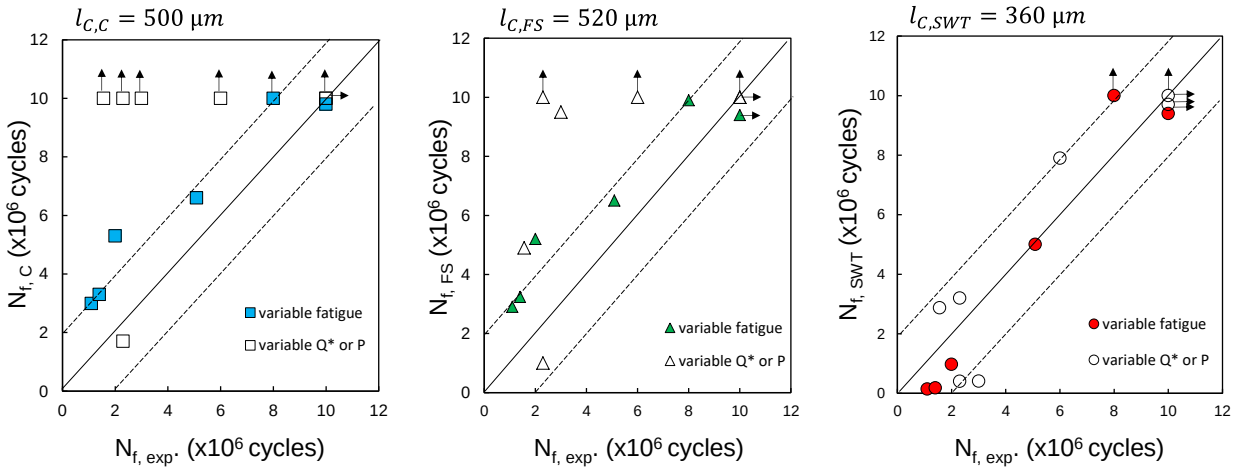

(a) *(b)* *(c)*

Fig. 13: Comparison between the experimental and predicted Fretting-Fatigue endurances: (a) Crossland criterion (Eq. 20, $l_{C,C}$ = 500µm); (b) Fatemi-Socie criterion (Eq. 21, $l_{C,FS}$ = 520 µm); (c) SWT criterion (Eq. 22).

- *Fatemi-Socie fatigue criterion*

A similar approach as that developed for the Crossland analysis is adopted. Hence, considering Eq. 12 and the critical distance method, Fatemi-Socie approach suggests that:

$$N_{f,FS} = \frac{1}{2} \exp\left(\frac{\ln\left(G.\frac{\Gamma_{FS}\left(l_{C,FS}\right)}{\tau_f'} \right)}{b} \right) \quad (21)$$

Figure 13b sums up the comparison between experimental and predicted endurances. Similarly to the Crossland criterion, a significant discrepancy is observed for tests with variable Q* or P, as well as many non-conservative predictions for both categories. Again the Fatemi-Socie criterion combined with the given non local $l_{C,FS}$ strategy seems non relevant to predict fretting-fatigue endurance at least for the studied configurations.

- *SWT fatigue criterion*

The lifetime estimation extrapolated from the SWT approaches is established by inverting Eq. 15 combining the critical distance strategy:

$$N_{f,SWT} = \frac{1}{2} \exp\left(\frac{\ln\left(E.\frac{\Gamma_{SWT}(l_{C,SWT})}{(\sigma_f')^2} \right)}{2b} \right) \quad (22)$$

Figure 13c compares the predicted endurances versus experiments. A lower discrepancy is observed suggesting that the SWT criterion combined with a $l_{C,SWT}$ = 360 µm critical distance strategy appears as the most relevant approach to predict the given fretting-fatigue endurances.

5.5 Discussion regarding the stability the critical distance approach

This combined experimental and simulation analysis revealed that both Crossland and Fatemi-Socie do not properly predict the experimental lifetime (Fig. 13 a,b). The use of a unique critical distance calibrated through a reference case seems not to be sufficient for these criteria to give robust and stable predictions in all cases. On the other hand, the same method applied with the SWT criterion gives much better results, with more robust predictions whether they are for variable fatigue tests or variable Q* or P tests (Fig. 13c). To better illustrate this aspect, a relative error index is calculated for every prediction displayed in figures 13a, b and c (table 3).

$$E\% = 100 \text{ x } \frac{|N_{f,pred} - N_{f,exp}|}{N_{f,exp}} \quad (23)$$

Where $N_{f,pred}$ corresponds to the predicted lifetime calculated through eq. (20), (21) or (22) for Crossland, Fatemi Soci and SWT approaches respectively, and N_{exp} is the experimental lifetime. Figure 14 plots the evolution of the relative error versus the corresponding experimental fretting-fatigue endurances.

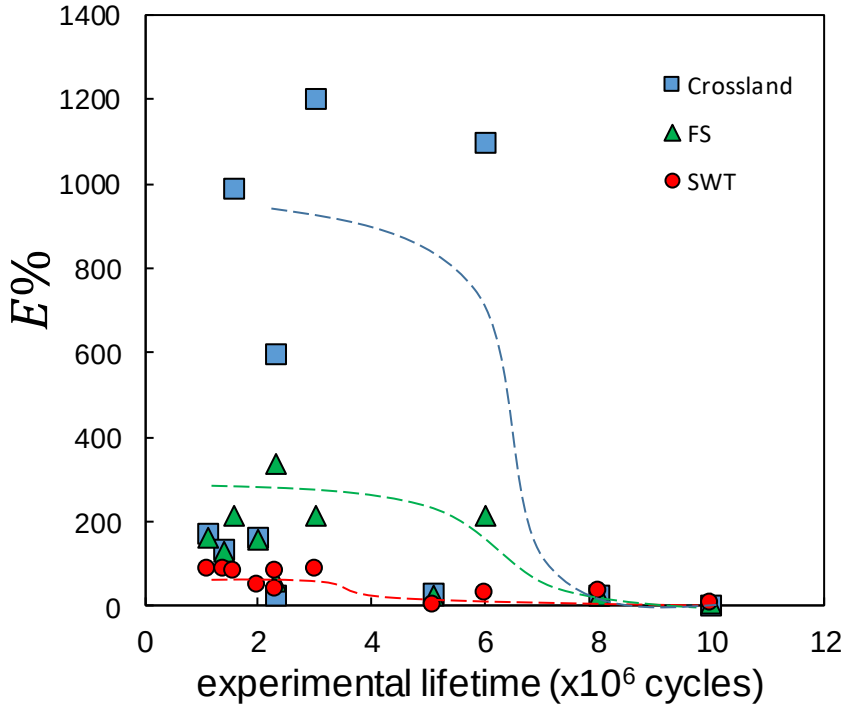

Fig. 14: prediction of the relative error E% versus the finite experimental lifetimes obtained for every simulation and every criterion used (the error was not calculated for experimental lifetimes exceeding 10^7 cycles).

As expected, the predictions in the long endurance range (i.e. N > 8 10^6 cycles) are rather good since the critical distances have been calibrated at the fretting-fatigue endurance limit of the variable fatigue stress experiments. However, very different discrepancy evolutions are observed in the medium endurance domain (i.e. < 8 million cycles). Although the SWT criterion maintains a low and stable scattering response with less than 100% error below 4 million cycles, both Crossland and FS criteria display a considerable rising in scattering. Typical sigmoid evolutions are observed showing a fast rising of *E*% with the decrease of the fretting-fatigue endurance. It reaches 300% for the FS criterion and more than 1000% for the Crossland approach. One explanation of this difference could be related to the formulation of the studied fatigue criteria. Indeed, both Crossland and FS criteria are based on shear mechanisms, and even though Crossland considers the hydrostatic stress influence, the computed α_C parameter is rather low with α_C = 0.3. These criteria are therefore appropriate to describe the incipient crack nucleation process as suggested in previous research where combining the Crossland criterion and the

critical distance made it possible to predict the 10 µm crack nucleation condition for low alloyed steel in [30] as well as the 70 µm crack length for Ti-6A-4V in [18].

By contrast, the SWT fatigue criterion derived from a finite endurance analysis better describes the propagating behavior by considering the principal stress $\sigma_{I,max}$ component. Hence, one hypothesis to explain the better results offered by the SWT formulation in the medium endurance range can be related to the fact that this fatigue criterion better takes into account the crack propagation stage and therefore better predicts the overall fretting-fatigue endurance. However, this assumption must be tempered: the crack propagation stage is usually significant for short endurance values (lower than 10^6 cycles) whereas the high endurance discrepancy is observed up to 6 million cycles in the current case. This means that even though the propagation aspect could partly explain the better predictions provided by the SWT criterion, other explanations must be considered.

A key aspect of the critical distance method is its capacity to palliate the stress gradient effect but also to describe the contact stress influence. On the other hand, the stability of the critical distance method must be discussed regarding the magnitude of the critical distance value versus the fretting stress field extension below the surface. Alternatively, the longer the critical distance, the smaller the influence of the contact stressing therefore the less captured the fretting stressing the crack nucleation process.

As mentioned previously, the strategy consisting in identifying the optimal critical distance applying a post-processing analysis of a reference condition is not new. It was first introduced to predict the crack nucleation risk under plain fretting condition [14], [15] then extended to fretting-fatigue conditions [17]. This strategy was successfully adopted to predict the fretting fatigue endurance for rather large contact size and medium stress gradient condition leading to optimal critical distance smaller than 200 µm [18]. Using this approach, lowly scattered crack nucleation predictions were achieved. To explain the present scattering, it must be underlined that the given analysis focuses on the cracking failure, involving very high stressing conditions. These conditions promote longer critical distances. The stress paths used at these critical distances to compute the cracking failure is therefore less representative of the contact fretting stressing.

One strategy to quantify the relative influence of the contact stressing as a function of the subsurface critical distance consists in comparing these latter versus the hydrostatic stress gradient $\nabla\sigma_H$ evolution below the surface hotspot (Fig. 15). Indeed, as the fatigue bulk stress is homogeneous, the fluctuation of the hydrostatic stress gradient only depends on the contact stress influence. For the current case, $\nabla\sigma_H$ is calculated in 1D along the z direction using the Euler explicit method.

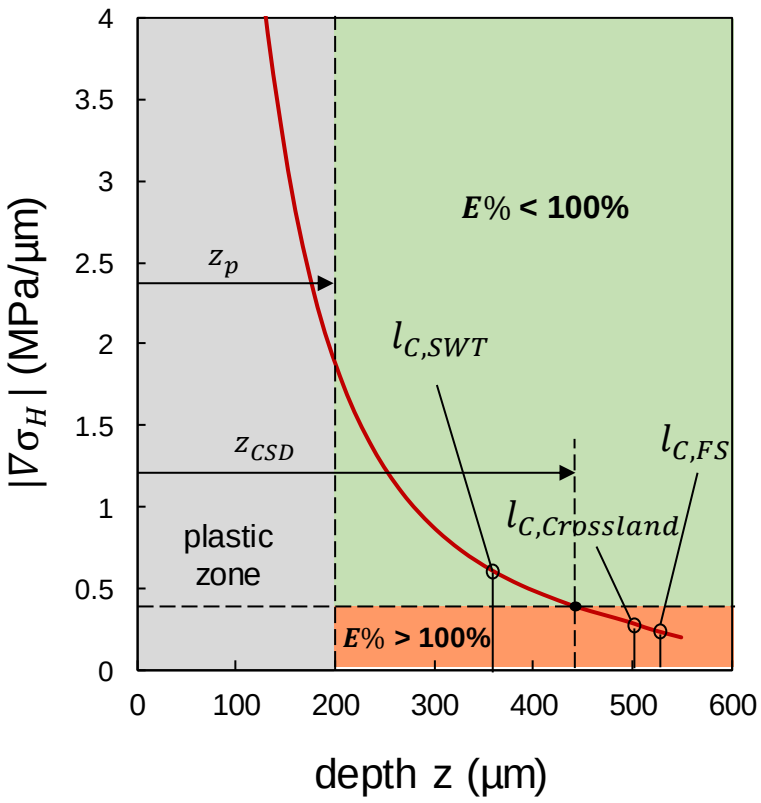

Fig. 15 : Evolution of the hydrostatic stress gradient $\nabla\sigma_H$ versus the depth z at the vertical of the trailing contact border (x=-a) (Related critical distances as function of the chosen fatigue criteria and corresponding E% error domains).

This plot highlights the following aspects:

All the critical distances are beyond the plastic influence domain which confirms *a posteriori* the relevance of the elastic assumption for the contact stress analysis.

The σ_H gradient values, computed at the $l_{C,C}$ = 500µm, $l_{C,FS}$ = 520 µm and $l_{C,SWT}$ = 360 µm critical distances, are equal to $\nabla\sigma_H(l_{C,C}) = 0.28$ MPa/µm, $\nabla\sigma_H(l_{C,FS}) = = 0.24$ MPa/µm and $\nabla\sigma_H(l_{C,SWT}) = 0.6$ MPa/µm respectively. Hence, the stress gradient at $l_{C,SWT}$ is more than twice the value related to Crossland and Fatemi-Soci critical distances. It can therefore be concluded that the shorter optimal critical distance extracted from the SWT post processing analysis allows a better description of the operating fretting stressing. Both crack nucleation and propagation processes can be captured and finally a better prediction of the fretting-fatigue endurance is obtained.

To support this hypothesis, the E% error index is plotted versus the stress gradient condition operating at the corresponding critical value (Fig. 16). Hence, for every point labeled "SWT", the corresponding gradient is $\nabla\sigma_H(l_{C,SWT})$ and the same has been applied for the two other fatigue

criteria. This $\nabla\sigma_H$- E% chart illustrates the previous arguments: the lower the stress gradient at the critical distance, the higher the discrepancy and the higher the prediction error.

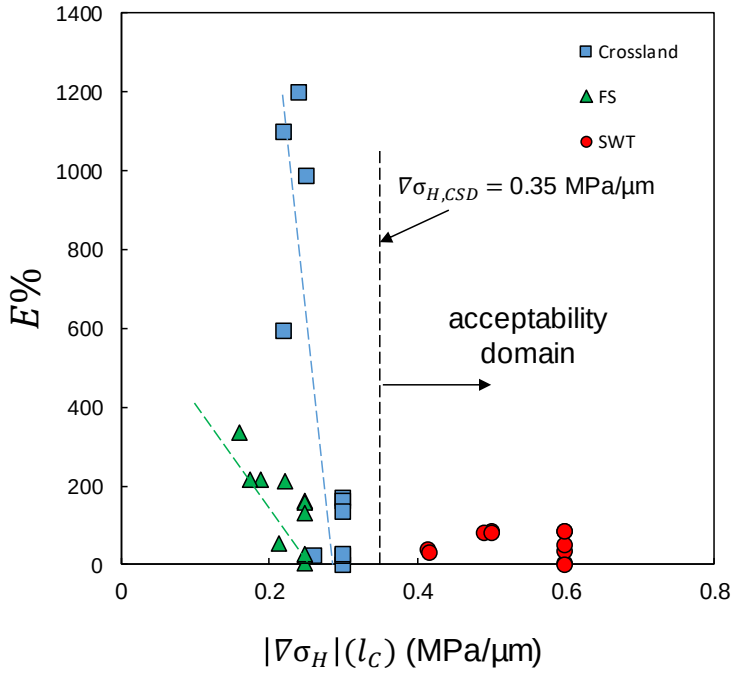

Fig. 16: Prediction relative error E% versus the hydrostatic stress gradient $\nabla\sigma_H$ for every simulation and every criterion used.

From this analysis it can be concluded that below a threshold stress gradient condition referred to as the threshold Contact Stress Description stress gradient condition (i.e. $\nabla\sigma_{H,CSD}$), estimated around 0.35 MPa/µm, the fretting stress is not sufficiently considered in the fatigue stress analysis comparatively to the bulk loading. The multiaxial fatigue stress - critical distance method is therefore no more reliable to predict the fretting-fatigue endurance.

On the other hands, the critical l_C must be long enough to avoid the subsurface plastic domain interference but short enough to capture the contact stressing.

For the studied condition, it leads to the following restrictive critical-distance condition:

- $l_C > z_p$ so that $\sigma_{VM(E)}(z_p) = \sigma_{VM(EP)}(z_p)$
- $l_C < z_{CSD}$ so that $\nabla\sigma_H(l_C) > \nabla\sigma_{H,CSD} \approx 0.35\ MPa/m$ (24)

Where z_p and z_{CSD} are the plastic and Contact Stress Description subsurface threshold depth, $\sigma_{VM(E)}$ the Von Mises stress computed using elastic hypothesis, $\sigma_{VM(EP)}$ the Von Mises stress computed using an elastoplastic hypothesis and $\nabla\sigma_{H,CSD}$ the associated hydrostatic stress gradient threshold. Obviously, such an analysis must be supported by additional investigations. However, this restrictive length scale condition appears as an interesting approach to calibrate the use of the critical distance method so as to avoid the effect of top surface plasticity and at the same time to

correctly consider the effect of contact stressing. Hence, if l_C is too short, the elastic stress computations are altered by the plastic deformation whereas if l_C is too long, the influence of the contact stressing will be minored comparatively to the bulk fatigue stress.

6. Application of the non-local optimal critical-distance approach to predict the fretting damage in clamped multi-strand cable structure subjected to vibrational bending loadings

The former analysis concludes that the fretting-fatigue cracking endurance of a crossed-wire mono-contact configuration can be predicted coupling a SWT multiaxial fatigue stress analysis with a critical distance method calibrated from the post processing analysis of the endurance limit achieved varying the fatigue stress whereas a constant representative fretting loading was applied (i.e. $\sigma_{HSWT}(l_{C,SWT})$ with $l_{C,SWT}$ = 360 µm. The next objective of this research work is to determine to what extent this approach is suitable to predict the fretting-fatigue cracking risk in real conductors (involving numerous crossed-wire contacts) when this latter is subjected to tensile and vibrating loadings. The study is based on the overhead conductor of the CROCUS 412 type. It is an ACSR type conductor made up of five layers of strands for a total of 51 strands (Fig. 17):

- The central strand and the first two layers (19 strands) are made of 2.4 mm diameter galvanized steel strands. As these layers generally show little or no damage, they have not been studied.

- The two outer layers are made up of a total of 32 quasi-pure 3.6 mm diameter 1XXX aluminum (strands similar to the ones investigated in the given mono-contact investigation) which are the targets of this investigation.

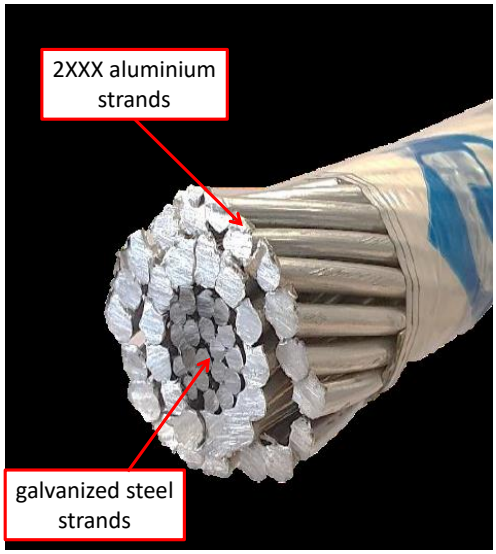

Fig. 17: Illustration of the studied CROCUS 412 conductor (cross section).

6.1. Overhead bending test experiments

The bending fatigue test of the clamped overhead conductor has been performed at the technological center of DERVAUX Company. This conductor-clamping test system is quite similar to the one developed by Kalombo *et al.* [31] although the boundary conditions and the load application are different by many aspects. Figure 18 illustrates the clamp assembly. In addition to the keeper and the support clamp geometries, a key aspect is the clamping force applied. To establish this value, one of the four tie rods was previously instrumented using strain gauges. It is

shown that for the reference torque value, the tension force applied to the tie rod is around 15 kN. Thus, considering the 4 tie rods, the support force exerted by the keeper on the 412 conductor is estimated at 60 kN.

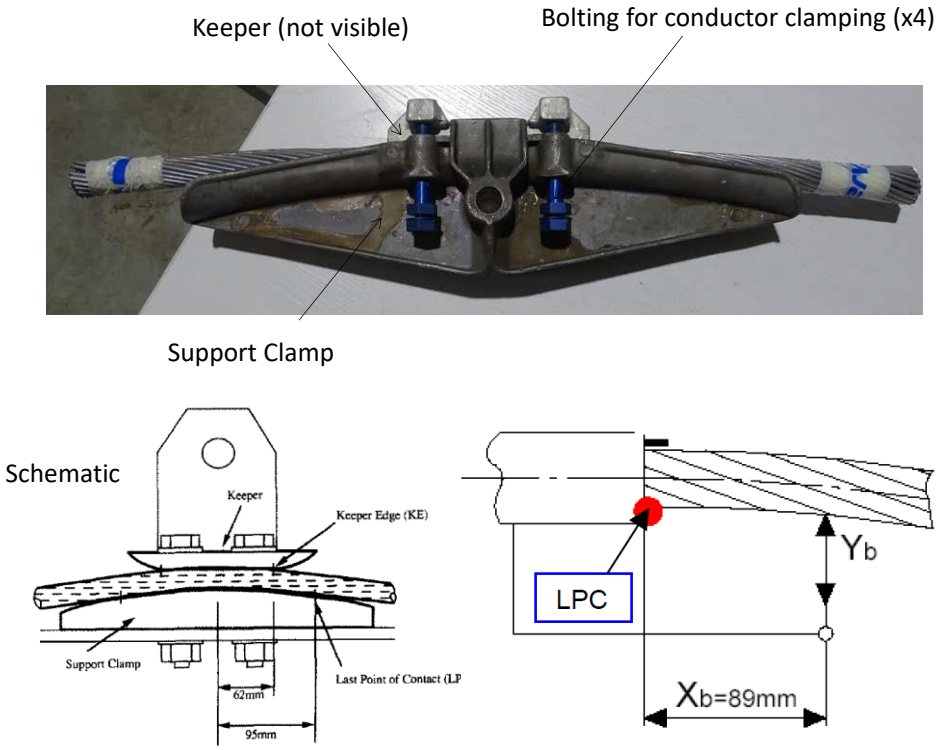

Fig. 18: Illustration of the studied CROCUS 412 clamping assembly.

Figure 19 provides a global overview of the vibrational conductor test. The clamping assembly is fixed at the middle position of the 30 m conductor for an active range of 14 m (the region subjected to vibration stresses). This latter is installed on an adjustable height turret allowing the application of a static angle of the conductor at both ends of the clamp: the higher the height of the clamp raised on the turret, the greater the angle of the static bending. Each end of the conductor is then fixed to lateral frames. Then, using hydraulic actuators, the static tension load is applied. For the studied condition, the latter was fixed at F_tension = 42.15 kN. An electromagnetic shaker is then positioned between the turret and the lateral frames to impose vibrations to the conductor.

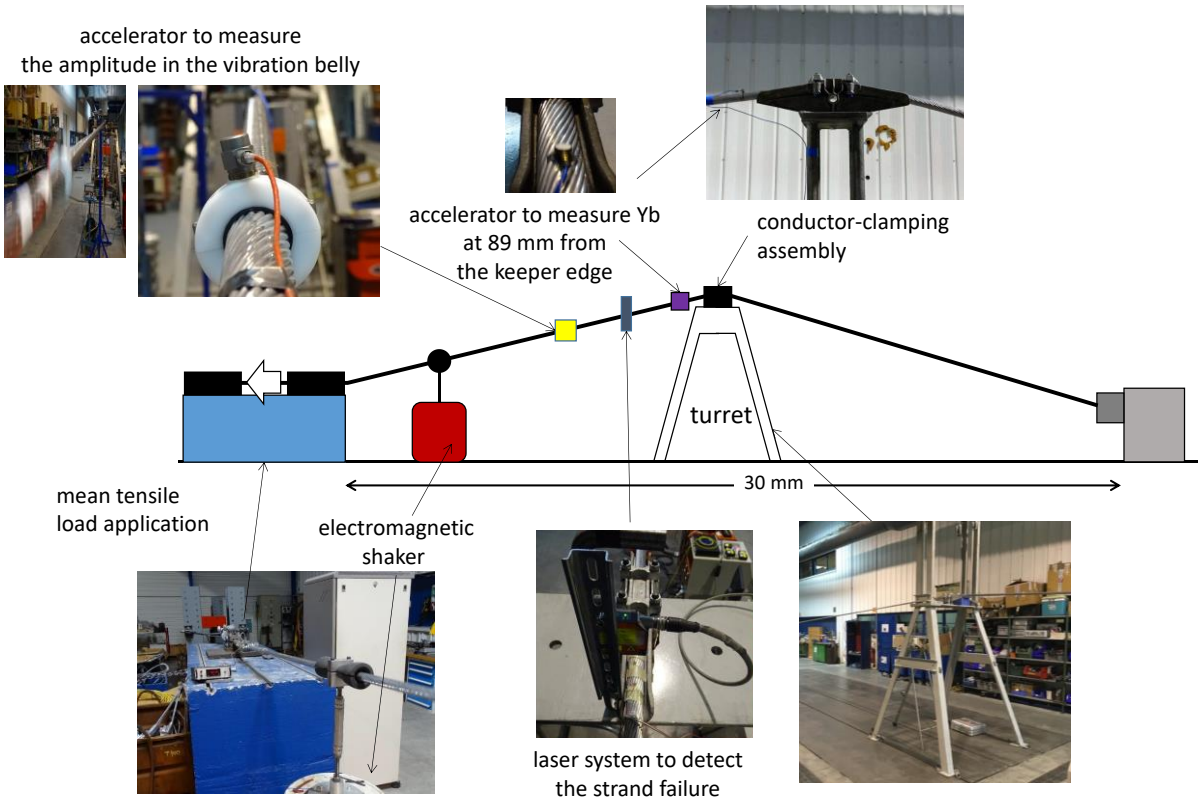

Fig. 19: Illustration of the DERVAUX's tension vibrating bending test system used to characterize the endurance of the CROCUS 412 clamping assembly including the instrumentation to control the loading conditions and detect the strand breaking occurrence.

An oscillating movement is then imposed by the electromagnetic shaker to ensure waves in the active range, with nodes and antinodes of vibrations. The amplitude is then controlled via three main measurement systems:

- A uniaxial accelerometer located on a vibration antinode: allows direct control of the vibration amplitude imposed on the CROCUS 412 conductor by the vibrating electro-shaker.

- A laser sensor located on a vibration node allows measuring the rotation of the conductor during the test. When a strand breaks, a slight rotation of the conductor occurs around its axis. The rotation measurement allows an *in situ* detection of the strand failure. Besides, due to the different winding angles of the two aluminum layers, the direction of rotation also makes it possible to deduce in which layer a break is occurring.

- A uniaxial accelerometer located at 89 mm from the last point of the contact: makes it possible to measure the deflection Yb which is commonly considered in the conductor industry to quantify the bending loading.

Hence, tests are displacement controlled based on two measurements: the displacement amplitude Yb measured 89 mm away from the Last Point of Contact with the clamp, as it is usually

recommended among TSOs recommendations, and Ymax the vibration amplitude measured at the antinode. The command applied on the electromagnetic shaker is adapted in order to reach the targeted values for Yb and/or Ymax, depending on the test. The applied loading conditions and the resulting damage measured after 10^7 vibrating cycles are compiled in table 4.

Table 4: Loading conditions and the resulting damage related to the DERVAUX's technological test on the studied CROCUS 412 clamping assembly.

tension force F_tension	42.15 kN
bending angle at rest (adjusted by the turret)	4°
bending angle at the maximum flexure loading φ_{max}	-13°
bending angle at the minimum flexure loading φ_{min}	+5°
standard amplitude of flexion Yb at 89 mm of LPC	± 1.25 mm
number of broken strands detected on the external layer (aluminum)	3
number of broken strands detected in the internal layer (aluminum)	2
applied vibrating cycles	10^7 cycles

6.2. Expertise of fretting fatigue damage

After the test, the conductor is cut on each side, the clamping system is removed and the damaged zone below the clamping keeper is inspected. Some strands are cut in order to investigate the internal part of the overhead. Figure 20 illustrates the principle of the damage expertise.

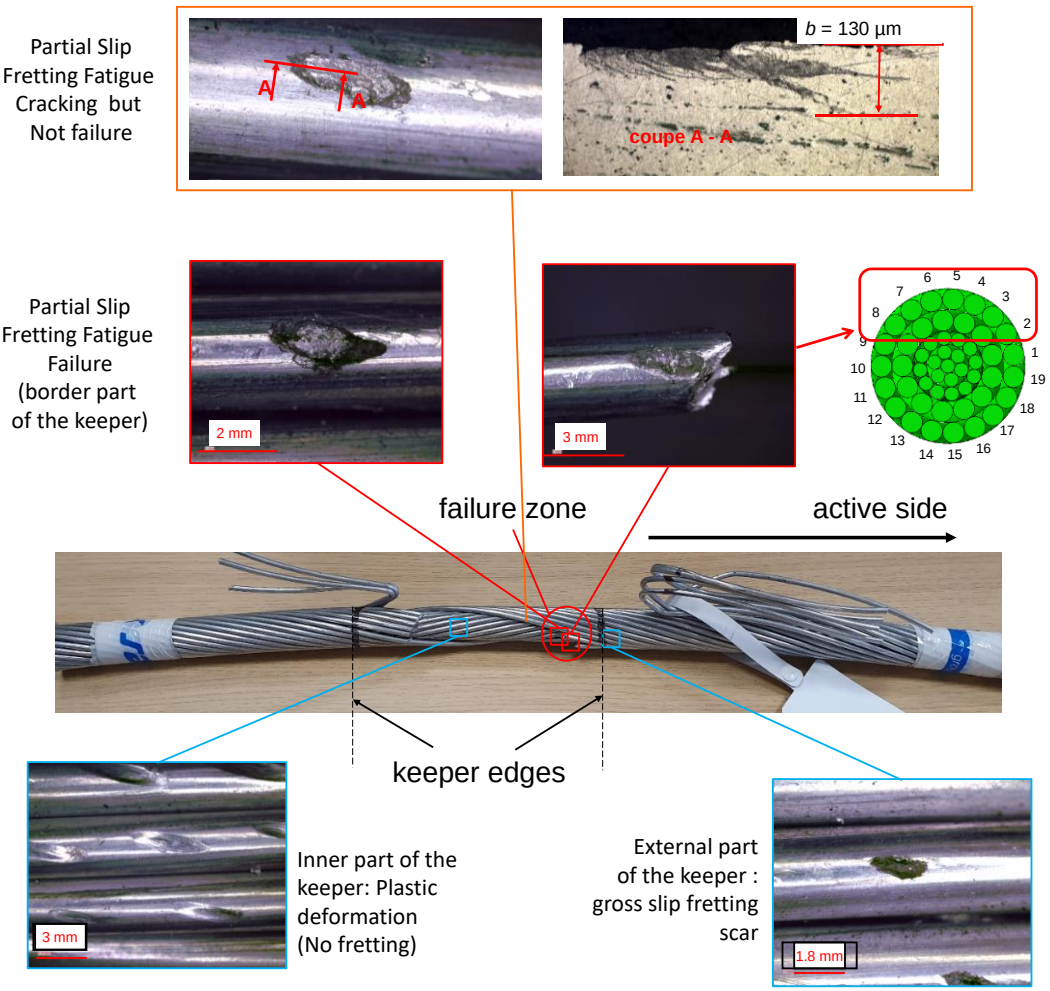

Fig. 20: Expertise of the fretting damage of the CROCUS 412 strands below the clamping assembly.

The expertise focuses on the top part of the overhead conductor (*i.e.* strand number from 2 to 8) where the maximum fretting sliding but also the maximum tensile fatigue stresses operate. In the middle part below the keeper, high contact pressures but rather small relative displacements are occurring. Significant plastic indents are observed but nearly no fretting scars are identified. Next to the keeper edge, on the side where the vibratory loading is applied, although the contact pressure decreases the relative displacement between strands increases. Numerous partial slip fretting scars characterized by inner undamaged stick zone surrounded by a corona of black oxides can be observed. These loading conditions favor dangerous fretting-fatigue cracking degradation. Outside the clamping assembly (the external part of the keeper), the contact pressure between the strands is drastically reduced although large displacement amplitudes operate. These loading conditions induce surface wear but the imposed contact stresses remain very low and do not promote any cracking risk. The expertise confirms that the five broken strands detected using the triaxial accelerometer were systematically related to partial slip fretting scars located in the active side around the keeper edge. Surface damage but also fracture morphologies are very similar to those observed using the mono-contact fretting experiments which *a posteriori*

confirms the representativeness of given mono-contact double actuator fretting-fatigue setup. Besides, the cracks are systematically located at the contact border of the fretting scar which again supports the SWT fatigue criterion which also predicts a maximum cracking risk at the contact edges.

6.3. Numerical simulation

The global assembly has been fully simulated using the numerical strategy detailed in [13] applying the loading and the boundary conditions related to the full scale experiment (Fig. 21). As detailed in [13], a parametric study confirms that the global FE model can be simplified using shell elements to simulate both support clamp and keeper elements. The simulation was done applying the loading conditions compiled in table 4, with F_tension= 42.15 kN and considering the two bending angles φ_{max} = -13° and φ_{min} = + 5°.

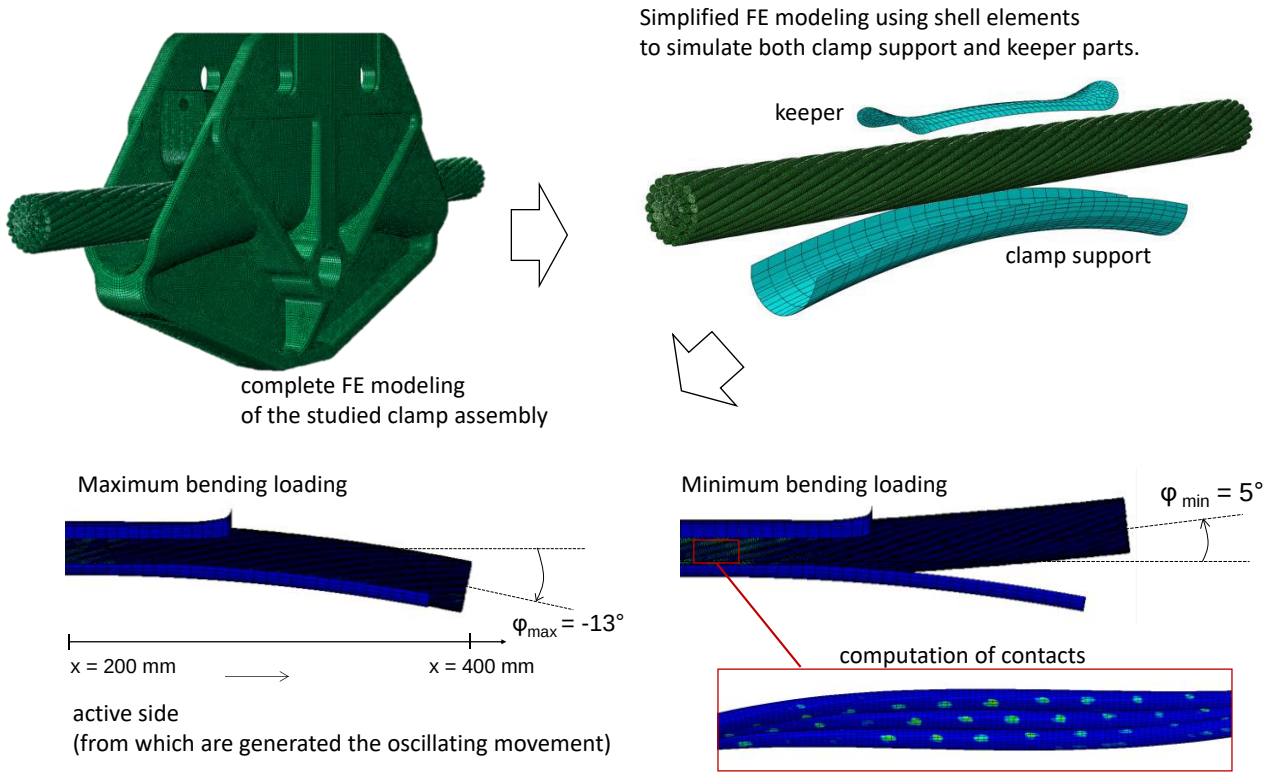

Fig. 21: Expertise of the fretting damage of the CROCUS 412 strands below the clamping assembly.

Figure 22 plots the evolution of the averaged stresses imposed at each extremum loading state to the outer aluminum strand of the overhead at X = 300 mm from the fixed left end of the assembly which means the right outside of the keeper. As expected, the maximum tensile stresses are observed on the top and bottom parts in strand numbers 5 to 8 and 14 to 17 respectively. On the top part, the stress varies from 120 to 60 MPa justifying the R= 0.5 fatigue stress ratio used for mono-contact fretting-fatigue experiments. The bottom stresses vary from +90 to -20 MPa. Hence, despite the application of significant mean tensile stress, some aluminum strands endure compressive stress state during the bending loading involving negative stress ratio. From this

analysis it can be concluded that the studied full scale test implies larger fatigue stress ranges than those investigated during the previous mono-contact fretting-fatigue experiments. However, these latter can be considered as representative because they correspond to the medium part of the load spectrum with a maximum stress up to 90 MPa and a load ratio R=0.5.

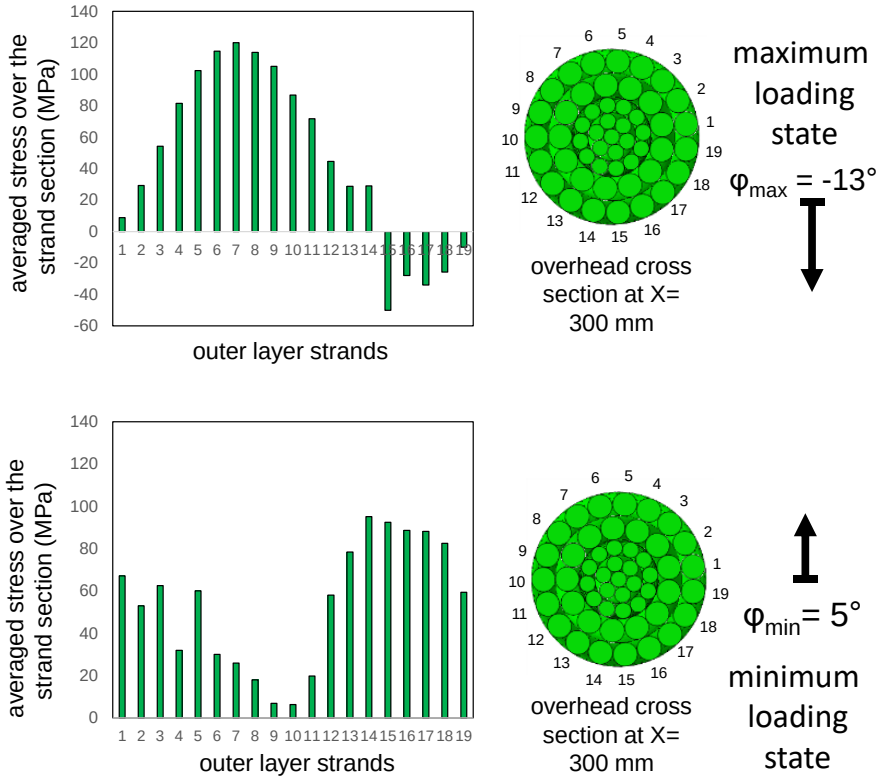

Fig. 22: Averaged stress imposed on the strands at X=300 mm for the two extremum loadings φ_{max} = -13° and φ_{min} = + 5° (mean rest position φ_{mean} = + 4°, F_tension= 42. 15 MPa) (border of the keeper X = 220).

Multi-Contact stress analysis

The python-abaqus subroutine introduced in [13] is applied to compute the whole distribution of the fretting loadings (i.e. the normal force P and the tangential force Q) related to all the strand contacts activated below and up to 100 mm outside the keeper assembly for the two loading states φ_{max} = -13° and φ_{min} = + 5° (Fig. 23). The tangential forces are plotted in green and the normal forces in red. Each point corresponds to the values computed for a contact between two aluminum strands at a given position. A total of 701 inter-strand contacts were detected from this simulation.

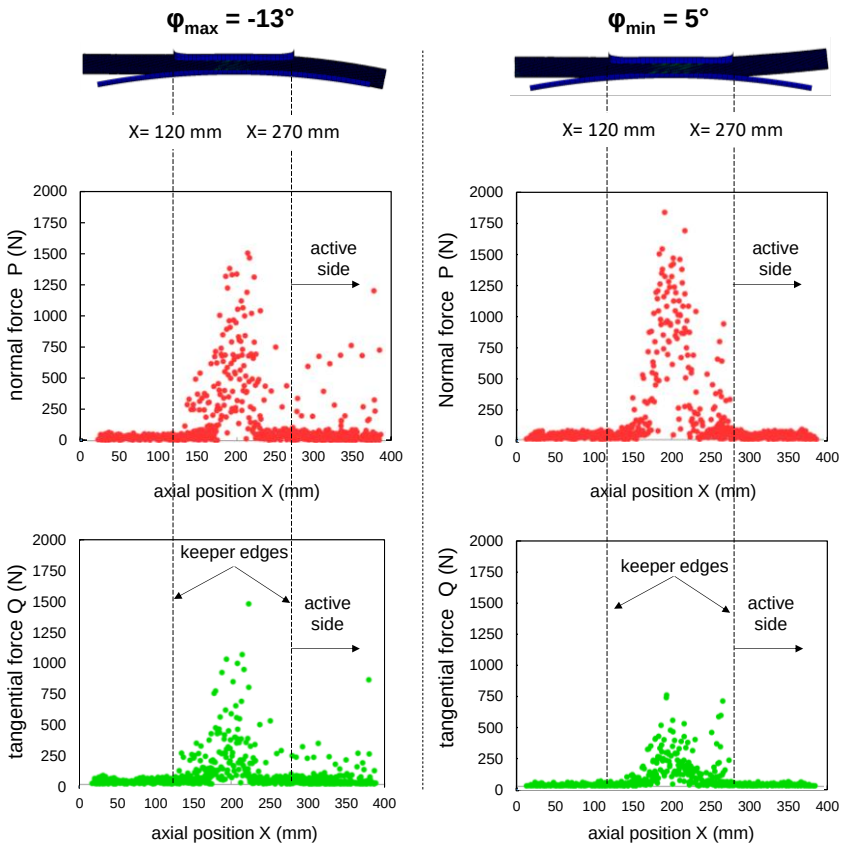

Fig. 23: Computation of the normal and tangential forces related to the aluminum strand contact between the two external and inner layer for the two extremum loading conditions φ_{max} = -13° and φ_{min} = + 5° (mean rest position φ_{mean} = + 4°, F_tension= 42. 15 MPa).

The maximum normal forces between the contacted crossed strands is observed in the central part of the assembly (*i.e.* 150 mm < X < 250 mm) reaching 1500 N. These very high values can explain the plastic indents observed in this region (Fig. 20). However, a second set of maximum normal forces reaching 1000 N is observed next to the keeper edge of the active side where partial slip and cracking phenomena were observed. Similar distributions were detected for φ_{max} = -13° and φ_{min} = + 5° which implies that the bending loading plays a minor effect regarding the normal force which is mainly monitored by the clamping force.

The most important aspect concerns the tangential force (Q) applied to the contact. The maximum values are observed in the inner part of the assembly but in fact the most important parameter is the variation of Q during the loading cycle (i.e. tangential force amplitude Q*(± N)) between φ_{max} = -13° and φ_{min} = + 5°. Globally, this latter is around Q*≈ 250 N in the central part of the assembly but similar values are also observed at the keeper edge domain since Q ≈ 750N when φ_{min} = + 5° decreasing to 250 N when φ_{max} = -13°. Hence, these rather high tangential force amplitudes combined with P ≈ 500 N medium normal force favor cracking partial slip conditions in the lateral part 250 mm < X < 270 mm of the keeper assembly.

Selection of most critical contacts and SWT fatigue stress analysis.

More than 701 contacts have been detected below the keeper assembly. Obviously, the complete FEM "mono-contact" fretting-fatigue stress analysis cannot be generalized to all of them. A screening procedure to select the most detrimental cases is therefore applied (Fig. 24).

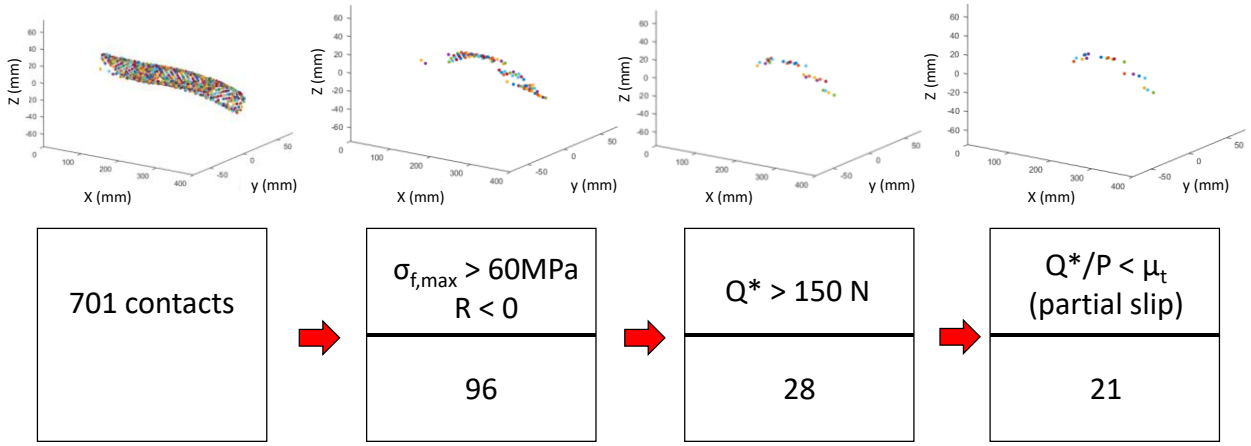

Fig. 24: Illustration of the screening *procedure to select the most detrimental strand contacts in the conductor below the keeper assembly.*

This latter first focuses on the severity of the fatigue stress experienced by the strands. Figure 22 suggests that strands 15 to 19 endure the highest fatigue stress loading. They are all characterized by $\sigma_{f,max} > 60$ MPa and a load ratio $R = \sigma_{f,min}/\sigma_{f,max} < 0$. According to this criterion, the number of contacts to be considered drops from 701 to 96. By adding a criterion on the tangential fretting force amplitude (i.e. Q* > 150 N), the number of the remaining contacts is reduced to 28. Finally, the last condition to retain the most critical fretting-fatigue contacts is the partial slip condition (i.e. $Q^*/P < \mu t$). Indeed, under gross slip, surface wear extends the contact area, reduces the contact pressure and shear stresses and finally decreases the cracking risk. The final number of contacts respecting all the conditions listed so far is thus 21 (Fig. 24). Among these 21 contacts, 5 particular contacts were chosen to be studied in more details. The associated stress conditions are noted in table 4, with the fretting loads Q* and P, as well as the fatigue loading deduced from figure 22 and 23. These contacts were chosen so as to be representative of all 21 isolated contacts in the macroscopic simulation. For each of these contacts, the fatigue loading was evaluated on the assumption that the contacts belonging to the same strand are subjected to the same core stresses as for instance for contacts 2 and 3 which both belong to the outer layer stand number 15 (Fig. 22).

Table 4: Selected fretting-fatigue contacts and the related FEM mono-contact SWT nonlocal fatigue stress analysis.

selected contacts	axial position X (mm)	Q* (N)	P (N)	$\sigma_{f,max}$ (MPa)	$\sigma_{f,mIN}$ (MPa)	$\frac{\sigma_{SWT}(l_{c,SWT})}{\sigma_d}$ failure if > 1	N_{pred} (x10^7 cycles)
1	152	211	314	88	-28	1.43	0.14

2	171	353	675	91	-50	1.41	0.16
3	230	317	1046	91	-50	0.96	>10
4	230	209	490	60	-10	0.81	>10
5	250	507	752	88	-34	2	<0.1

Each of these selected loading conditions has been simulated using the FEM mono-contact model applying the corresponding loading condition. Then, the nonlocal SWT fatigue stress analysis at the optimal critical distance $l_{C,SWT}$ = 360 µm has been performed. The model predicts failure when $\sigma_{SWT}(x = -a;\ z = l_{C,SWT}) > \sigma_d$ = 65 MPa for contacts 1, 2 and 5 and no failure for contact 3 and 4. The number of cycles to failure can be estimated using the Basquin-Coffin-Manson law described in section 5 (Eq. 22). These 5 representative contacts are positioned according to their x and y positions of the assembly in figure 25.

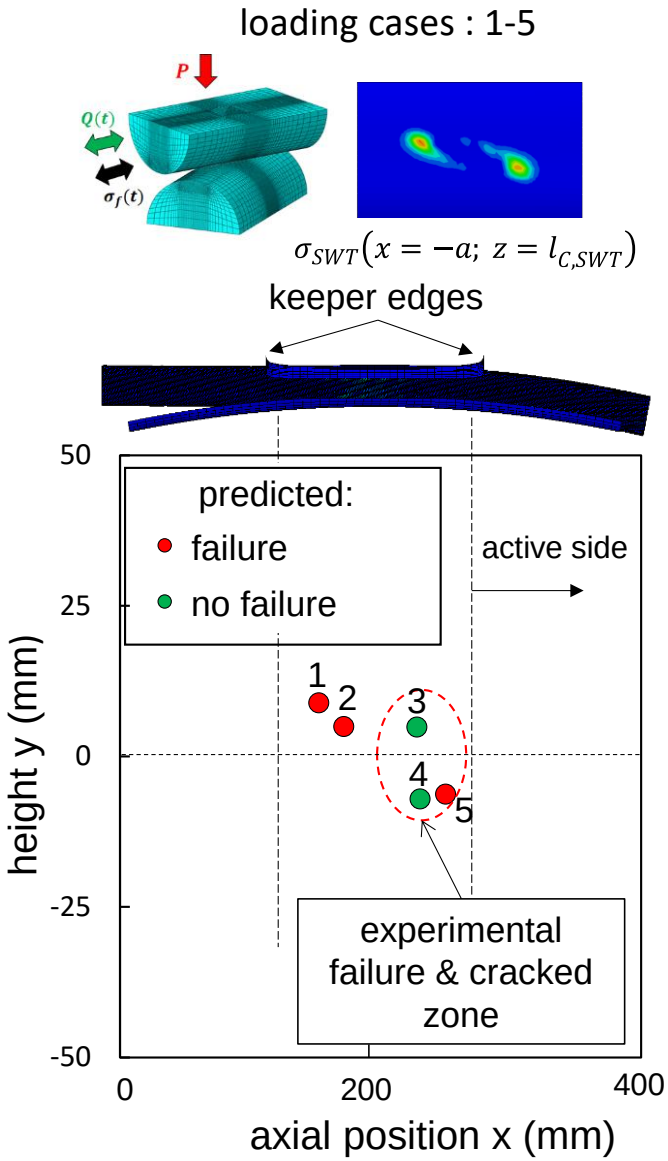

Fig. 25: Computation of SWT nonlocal fatigue stress of the selected representative contacts (1 to 5) (Table 4) and the related x and y positioning of these latter.

Based on this fatigue criterion, failure is predicted for three of the five selected contacts. More than 50% of them are likely to break before 10^7 cycles. By extrapolation to the initial set of 21 contacts, the model is expected to predict more than 10 strand failures. Compared to the 3 experimental strand failures, it can be concluded that the given model is quite conservative. This overestimation could be explained by the given assumption and more particularly by the elastic hypothesis which tends to overestimate the fretting-fatigue stress field although this aspect is partly tempered by the critical distance strategy. This underlines that future developments need to better consider the cyclic plastic response of the studied material. Note that the given cyclic plastic law, estimated from conventional tension-compression law (see section 2.2), is partly representative because it does not take into account the high compressive stress state imposed by the fretting contact. More elaborated strategies including the simulation of fretting scars [32] in the identification procedure need to be considered to extract more representative cyclic plastic law. Another aspect concerns the screening procedure which can be greatly improved by refining the criteria for selecting the most severe contacts. This optimization, however, requires additional overhead bending tests varying the boundary condition but also the clamping force, the tension force imposed on the conductor and the loading angles. Nevertheless, despite its limitations and the strong hypotheses assumed, the given Global-Local Fretting-Fatigue strategy, based on a post processing identification of the critical distance from adequate fretting-fatigue experiments, appears quite reliable. FEM computations can easily be automated and moreover the predictions seem sufficiently conservative to provide safe conductor/clamping designing. Note that an alternative general life estimation strategy was recently introduced by Rocha et al. [33]. However, the work presented here is characterized by two original features, namely the identification of an optimized critical distance to capture the stress gradient effect and the development of an original screening criterion to most detrimental strands contacts.

7. Conclusion

The present work proposes a global-local approach to predict the lifetime of aluminum strands subjected to fretting-fatigue loadings within an overhead conductor. Figure 26 illustrates the principle of this modeling strategy.

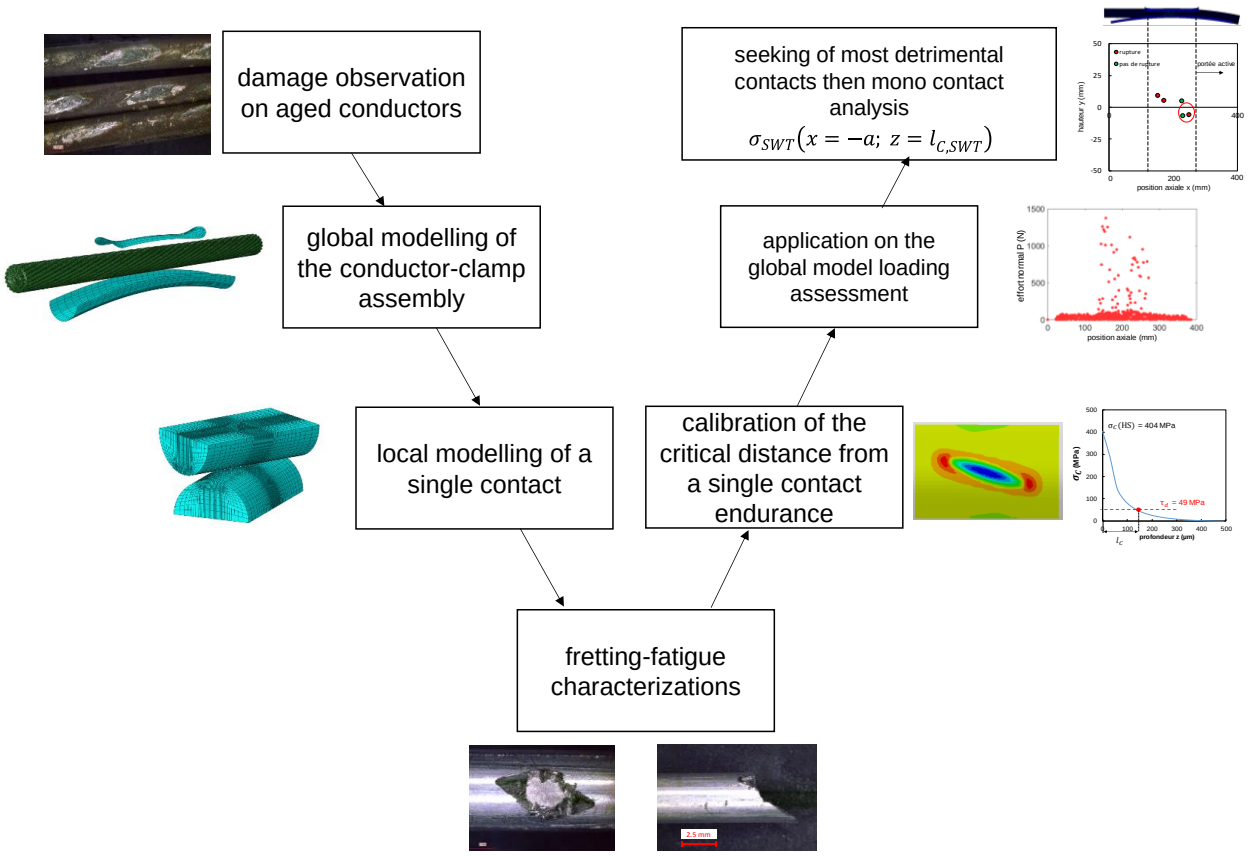

Fig. 26: Illustration of the global-local approach applied to predict the fretting-fatigue damage in an overhead conductor.

The following aspects were developed and exposed:

- A first 3D modeling of the entire conductor allowed us to frame the loading spectrum (i.e. fatigue stress, normal and tangential forces) imposed on the crossed 1XXX strand contacts below the clamping assembly. Knowing these loading condition, mono-contact fretting-fatigue experiments were carried out by studying the effect of the fatigue stress, normal force as well as the contact tangential force amplitudes.

- The analysis of failed and unfailed mono-contact samples helped to characterize the cracking mechanisms. Nucleated cracks on unfailed samples always display the same orientation angle θ_{exp} = 60°, and SEM observations on a fracture surface revealed various fatigue-induced morphologies.

- The numerical model used to simulate a single contact has been recalled. It has been used with a material law experimentally identified taking into account combined non-linear kinetic and isotropic hardening. The difference between elastic and plastic modeling was then emphasized in terms of Von Mises equivalent stress. Although the plastic flow cannot be neglected close to the contact surface, a non-local analysis with a purely-elastic condition can be applied as long as the critical distance is larger than z_p = 200 µm.

- Three fatigue criteria were applied: the Crossland invariant-based formulation as well as the SWT and FS critical plane criteria. The associated critical distances were calibrated through the post-processing of a single fretting-fatigue test, and were found at $l_{C,Crossland}$ = 500 µm, $l_{C,SWT}$ = 360 µm and $l_{C,FS}$ = 520 µm, respectively. The lifetime predictions achieved using these three formulations showed that SWT managed to return realistic estimates while being rather conservative for lower lifetimes. On the contrary, Crossland and FS displayed a much higher discrepancy and did not return good predictions for all tested cases.

- The difference in performances between SWT and the shear-based criteria FS and Crossland were discussed. The best predictions achieved using the SWT criterion can be explained by the fact that SWT offers a better assessment of the crack propagation driven by the principal stress σ_I (mode I). However, this investigation also suggests that the stability of the critical distance also depends on the physical length of this latter. The longer l_c, the less influent the contact stressing and therefore the less reliable the prediction. This aspect was quantified considering the hydrostatic stress gradient $\nabla\sigma_H$ at the critical distance considered. For a given critical distance l_C, the associated fatigue criterion can be applied as long as $\nabla\sigma_H(l_C) > \nabla\sigma_{H,th}$. Lower gradients at the critical distance would imply that the influence of the fretting contact is too weak to be captured by the criterion. This threshold was evaluated between 0.3 MPa.m$^{1/2}$ < $\nabla\sigma_{H,th}$ < 0.4 MPa.m$^{1/2}$. To conclude, an optimized critical distance (calibrated by post processing fretting-fatigue experiments) needs to be long enough to avoid the plastic effect operating on the top surface but also short enough to capture the fretting stress field and not only the plain fatigue loading. The best compromise for the studied contacts is achieved with the SWT fatigue approach (i.e. $\sigma_{SWT}(x = -a;\ z = l_{C,SWT})$ with $l_{C,SWT}$ = 360 µm > z_p = 200 µm).

- A vibration test on a complete conductor was carried out in the laboratory and then appraised, with a view to being simulated using the given Global-Local model. This technological test lasted 10 million cycles, and three breakages were observed on the strands of the outer layer. This test was simulated using a global model. Using this Global FEM model more than 701 strand contacts were detected. A dedicated screening procedure combining the effect of fatigue stress, tangential force amplitude but also the sliding condition operating to each of them is introduced. Using this screening procedure, 21 "most detrimental" contacts were detected. A set of 5 representative contacts among the 21 detected was simulated using the mono-contact nonlocal SWT fatigue stress analysis (i.e. $\sigma_{SWT}(x = -a;\ z = l_{C,SWT})$). This nonlocal SWT fatigue stress analysis confirms the prediction of 3 failures which reported to the 21 most detrimental cases. This infers that more than 10 failures are predicted by the model. Compared to the 3 experimental detected failures, the model is conservative.

Despite its limitations and the strong assumptions made, the given global-local fretting-fatigue strategy, based on a post processing identification of the optimal critical distance from adequate fretting-fatigue experiments, appears quite reliable. FEM computations can be easily automated and moreover the predictions seem sufficiently conservative to provide safe conductor/clamping designs. However, this version of the model can be significantly improved by better considering plasticity in the mono-contact non-local fatigue stress analysis but also by improving the screening procedure by comparing new overhead bending test experiments.

References

[1] W. G. Fricke and C. B. Rawlins, “Importance of Fretting in Vibration Failures of Stranded Conductors,” *IEEE Trans. Power Appar. Syst.*, vol. 87, no. 6, pp. 1381–1384, 1968.

[2] R. B. Kalombo, J. A. Araújo, J. L. A. Ferreira, C. R. M. da Silva, R. Alencar, and A. R. Capra, “Assessment of the fatigue failure of an All Aluminium Alloy Cable (AAAC) for a 230 kV transmission line in the Center-West of Brazil,” *Eng. Fail. Anal.*, vol. 61, no. August 2012, pp. 77–87, 2016.

[3] Z. R. Zhou, A. Cardou, M. Fiset, and S. Goudreau, “Fretting fatigue in electrical transmission lines,” *Wear*, vol. 173, no. 1–2, pp. 179–188, 1994.

[4] Z. R. Zhou, A. Cardou, S. Goudreau, and M. Fiset, “Fretting Patterns in a Conductor–Clamp Contact Zone,” *Fatigue Fract. Eng. Mater. Struct.*, vol. 17, no. 6, pp. 661–669, 1994.

[5] S. Lalonde, R. Guilbault, and S. Langlois, “Numerical analysis of ACSR conductor-clamp systems undergoing wind-induced cyclic loads,” *IEEE Trans. Power Deliv.*, vol. 33, no. 4, pp. 1518–1526, 2018.

[6] G. E. Ramey and J. S. Townsend, “Effects of clamps on fatigue of ACSR conductors,” *J. Energy Div.*, vol. 107, no. 1, pp. 103–119, 1981.

[7] A. Cardou, L. Cloutier, J. Lanteigne, and P. M’Boup, “Fatigue strength characterization of ACSR electrical conductors at suspension clamps,” *Electr. Power Syst. Res.*, vol. 19, no. 1, pp. 61–71, 1990.

[8] Z. R. Zhou, A. Cardou, S. Goudreau, and M. Fiset, “Fundamental investigations of electrical conductor fretting fatigue,” *Tribol. Int.*, vol. 29, no. 3, pp. 221–232, 1996.

[9] J. A. Araújo, F. C. Castro, I. M. Matos, and R. A. Cardoso, “Life prediction in multiaxial high cycle fretting fatigue,” *Int. J. Fatigue*, vol. 134, no. January, p. 105504, 2020.

[10] I. M. Matos, P. H. C. Rocha, R. B. Kalombo, L. A. C. M. Veloso, J. A. Araújo, and F. C. Castro, “Fretting fatigue of 6201 aluminum alloy wires of overhead conductors,” *Int. J. Fatigue*, vol. 141, no. August, p. 105884, 2020.

[11] I. M. Matos, J. A. Araújo, and F. C. Castro, “Fretting fatigue performance and life prediction of 1120 aluminum alloy wires of overhead conductors,” *Theor. Appl. Fract. Mech.*, vol. 121, no. April, p. 103521, 2022.

[12] M. A. Garcia, L. A. Mendes Veloso, F. Comes de Castro, J. A. Araújo, J. L. A. Ferreira, and C. R. Moreira da Silva, “Experimental device for fretting fatigue tests in 6201 aluminum alloy wires from overhead conductors,” *Wear*, vol. 460–461, no. August, 2020.

[13] J. Said, S. Garcin, S. Fouvry, G. Cailletaud, C. Yang, and F. Hafid, “A multi-scale strategy to predict fretting-fatigue endurance of overhead conductors,” *Tribol. Int.*, p. 106053, 2019.

[14] S. Fouvry, P. Kapsa, F. Sidoroff, and L. Vincent, “Identification of the characteristic length scale for fatigue cracking in fretting contacts,” *J. Phys. IV JP*, vol. 8, no. 8, pp. 2–9,

1998.

[15] S. Fouvry, P. Kapsa, and L. Vincent, “A Multiaxial Fatigue Analysis of Fretting Contact Taking into Account the Size Effect,” *ASTM Spec. Tech. Publ.*, vol. 1367, pp. 167–182, 2000.

[16] S. Fouvry, K. Elleuch, and G. Simeon, “Prediction of crack initiation under partial slip fretting conditions,” *J. strain Anal.*, vol. 75, no. 7, pp. 1763–1778, 2002.

[17] J. A. Araújo, L. Susmel, D. Taylor, J. C. T. Ferro, and J. L. A. Ferreira, “On the prediction of high-cycle fretting fatigue strength: Theory of critical distances vs. hot-spot approach,” *Eng. Fract. Mech.*, vol. 75, no. 7, pp. 1763–1778, 2008.

[18] R. Ferré, S. Fouvry, B. Berthel, and J. A. Ruiz-Sabariego, “Stress gradient effect on the crack nucleation process of a Ti-6Al-4V titanium alloy under fretting loading: Comparison between non-local fatigue approaches,” *Int. J. Fatigue*, vol. 54, pp. 56–67, 2013.

[19] D. Taylor, “The theory of critical distances,” vol. 75, pp. 1696–1705, 2008.

[20] J. A. Araújo, L. Susmel, D. Taylor, J. C. T. Ferro, and E. N. Mamiya, “On the use of the Theory of Critical Distances and the Modified Wöhler Curve Method to estimate fretting fatigue strength of cylindrical contacts,” *Int. J. Fatigue*, vol. 29, no. 1, pp. 95–107, 2007.

[21] K. Dang-Van, “Macro-micro approach in high-cycle multiaxial fatigue,” *Adv. multiaxial fatigue. ASTM Int.*, 1993.

[22] S. Kitagawa, H., Takahashi, “Application of fracture mechanics to very small cracks or the cracks in early stage,” *Proc. 2nd ICM, Clevel.*, pp. 627–631, 1976.

[23] J. Said, S. Fouvry, G. Cailletaud, C. Yang, and F. Hafid, “Shear driven crack arrest investigation under compressive state: Prediction of fretting fatigue failure of aluminium strands,” *Int. J. Fatigue*, vol. 136, no. March, p. 105589, 2020.

[24] R. Waterhouse, “Fretting in Steel Ropes and Cables — A Review,” *Fretting Fatigue: Advances in Basic Understanding and Applications*. pp. 3-3–12, 2008.

[25] W. Maktouf, K. Ammar, I. Ben Naceur, and K. Saï, “Multiaxial high-cycle fatigue criteria and life prediction: Application to gas turbine blade,” *Int. J. Fatigue*, vol. 92, pp. 25–35, 2016.

[26] J. M. Voisin, A. B. Vannes, L. Vincent, J. Daviot, and B. Giraud, “Analysis of a tube-grid oscillatory contact: methodology for the selection of superficial treatments,” *Wear*, vol. 181–183, no. PART 2, pp. 826–832, 1995.

[27] D. Nowell and J. A. Araújo, “The effect of rapidly varying contact stress fields on fretting fatigue,” *Int. J. Fatigue*, vol. 24, no. 7, pp. 763–775, 2002.

[28] R. Neu, J. A. . Pape, and D. Swalla, “Methodologies for linking nucleation and propagation approaches for predicting life under fretting fatigue,” *ASTM Spec. Tech. Publ.*, no. 1367, pp. 369–388, 2000.

[29] F. C. Castro, J. A. Araújo, and N. Zouain, “On the application of multiaxial high-cycle fatigue criteria using the theory of critical distances,” *Eng. Fract. Mech.*, vol. 76, no. 4, pp.

512–524, 2009.

[30] S. Fouvry, H. Gallien, and B. Berthel, “From uni- to multi-axial fretting-fatigue crack nucleation: Development of a stress-gradient-dependent critical distance approach,” *Int. J. Fatigue*, vol. 62, pp. 194–209, 2014.

[31] R. B. Kalombo, G. Reinke, T. B. Miranda, J. L. A. Ferreira, C. R. M. Da Silva, and J. A. Araújo, “Experimental Study of the Fatigue Performance of Overhead Pure Aluminium Cables,” *Procedia Struct. Integr.*, vol. 19, pp. 688–697, 2019.

[32] P. Arnaud, V. Maurel, S. Fouvry, J. Said, C. Yang, and F. Hafid, “Fretting tests for cyclic plastic law identification: application to a 1XXX aluminium crossed wire contact,” *Tribol. Int.*, 2022.

[33] P. H. C. Rocha, S. Langlois, S. Lalonde, J. A. Araújo, and F. C. Castro, “A general life estimation method for overhead conductors based on fretting fatigue behavior of wires,” *Theor. Appl. Fract. Mech.*, vol. 121, no. June, p. 103443, 2022.